

# We are IntechOpen, the world's leading publisher of Open Access books Built by scientists, for scientists

6,300

Open access books available

171,000

International authors and editors

190M

Downloads

Our authors are among the

154

Countries delivered to

TOP 1%

most cited scientists

12.2%

Contributors from top 500 universities



WEB OF SCIENCE™

Selection of our books indexed in the Book Citation Index  
in Web of Science™ Core Collection (BKCI)

Interested in publishing with us?  
Contact [book.department@intechopen.com](mailto:book.department@intechopen.com)

Numbers displayed above are based on latest data collected.  
For more information visit [www.intechopen.com](http://www.intechopen.com)



---

# Modeling of the Plasma 3D Deposition of Wire Materials

---

Dmitriy Trushnikov, Oleg Smetannikov,  
Anatoly Perminov, Shengyong Pang,  
Karuppasamy Poolan Karunakaran, Petr Maksimov,  
Mariia Bartolomey, Aleksei Kovyazin,  
Vladimir Belenkiy and Yurii Schitsyn

Additional information is available at the end of the chapter

<http://dx.doi.org/10.5772/intechopen.77153>

---

## Abstract

The numerical modeling of the physical process of manufacturing parts using additive technologies is complex and needs to consider a variety of thermomechanical behavior. This is connected with the extensive use of the finite element computer simulation by means of specialized software packages that implement mathematical models of the processes. The algorithm of calculation of nonstationary temperature fields and stress-strain state of the structure during the process of 3D deposition of wire materials developed and implemented in ANSYS is considered in the paper. The verification of the developed numerical algorithm for solving three-dimensional problem of the production of metal products using arc 3D deposition of wire materials with the results of the experiment is carried out. The data obtained from calculations on the developed numerical model are in good agreement with the experiment.

**Keywords:** wire deposition, thermomechanical behavior, additive technologies

---

## 1. Introduction

Additive technologies are a breakthrough solution of this century. At the same time, when we speak about additive technologies, we generally mean the manufacturing of products of small sizes and irregular shapes. Large-sized products are still characterized by the use of traditional casting and forging shops. If mass production, such as the motor vehicle industry, is generally

---

satisfied with traditional solutions, then small-scale manufacturing, such as the aircraft industry, requires a more advanced approach. A manufacturing cycle of relatively simple and large-sized products, such as longerons, frame elements, etc., may in certain cases take 2 years at a cost of 1.2 million dollars. The situation at hand is one of those reasons which result in unreasonably long terms and high costs of creation and introduction of new products to the market.

The use of powder additive technologies sometimes gives rise to problems associated with low productivity of existing methods, high costs of equipment being used, limited types of materials, which is caused by the fact that powder systems melted by a powerful thermal source [1–3] are traditionally used as initial materials for additive formation of products. The formation of products from many aluminum alloys and active metal alloys, such as titanium and magnesium alloys, leads to increased porosity of materials of resulted products with considerably decreased mechanical properties [4–7]. The productivity of formation of components from powder materials in traditional additive technologies is extremely low, which practically excludes any prospects of the use of these technologies for the purpose of manufacturing large-sized products.

Hybrid manufacturing technologies combine the best characteristics of additive formation of workpieces and those of subsequent mechanical removal of materials in the course of creation of metal products [8, 9]. This process can be implemented on one platform with the hybrid layer-by-layer application of wire materials and the processing by CNC machines and is an optimum solution for the manufacturing of large-sized components of molds of low and average complexity.

One of the first companies that is engaged in promoting wire material-related technologies is Sciaky (USA) [1, 2] that specializes in the development of electron-beam welding technologies and equipment. Additive manufacturing machines made by Sciaky produce components with the use of the layer-by-layer build-up welding method for materials in melts created by an electronic beam. This technology is known as EBDM (Electron Beam Direct Manufacturing). High performance levels (3–9 kg/h) demonstrated by the EBDM technology allow us to prepare components whose sizes are expressed in meters, which is impossible or extremely expensive when using any other additive technologies. This component formation principle is responsible for a low-quality surface of a synthesized component. However, the EBDM technology combined with traditional machining technologies allows us to obtain results with acceptable costs. Model materials used in this technology are additions (metal bars or wires), which is also an advantage as there are many available materials of this kind: nickel alloys, stainless and instrument steels, Co-Cr alloys and many others whose prices are considerably lower than those of these materials in their powdered condition [1]. Today, the company does not make standard machines and is generally involved in producing basic Sciaky's DM models with the sizes of a formation zone of  $5700 \times 1200 \times 1200$  mm, and all modifications are created according to customer requirements. Machines allow to consistently form up to 10 various components in automatic mode and during one vacuumization cycle of a working chamber. The price of one machine is more than \$2.0 million.

The use of arc and plasma sources for the purpose of melting metal wire materials in the course of implementation of hybrid additive manufacturing technologies has been actively developed

in recent years. In 2016, Norsk Titanium, a Norwegian start-up, attracted additional investments of 25 million dollars in order to certify materials resulted from the plasma layer-by-layer deposition with titanium wire and used to produce components for Boeing and Airbus aircrafts. It is also necessary to mention a company called WAAM (at Cranfield University) that is engaged in developing large-sized product formation technologies with the use of plasma technologies or consumable electrode surface welding processes with impulsive wire feeds and cold metal transfers (CMT) developed by Fronius. In the middle of 2016, Europe witnessed a 3-year LASSIM project with a budget of about 5 million euros that united 16 companies. The purpose of this project is to create a stand in order to implement several processes within a single space in the course of hybrid manufacturing of large-sized workpieces: additive manufacturing; multi-coordinate machining; layer-by-layer work hardening, measurement; non-destructive testing.

When modeling heat and mass transfer processes, it is necessary to consider that additive technologies are technologically closest to multi-layer deposition that also makes an initial material (filler wire) interact with a heat source, gradually builds up layers and superposes thermal cycles as and when new layers are added and transitional changes occur in the geometry. Temperature fields in a product to be processed are in most cases difficult to determine with the use of experimental methods. The most frequently used temperature measurement method consists in placing thermocouples directly next to the area of influence by a thermal source [10–13]. Thermocouples can measure temperatures only in places where they are installed, and it is difficult to have a general picture of temperature distribution even when several thermocouples are used. Infrared thermography [14–17] can measure only surface temperatures and cannot ensure the distribution of transient temperature processes in volume. The volume distribution of temperatures in a workpiece can be determined by mathematical modeling. However, the modeling of three-dimensional temperature fields is a rather demanding and complex problem due to accompanying difficult physical processes, their velocities, and many previously made calculations are connected with simplifications [18–21].

In order to model heat and mass transfer processes, we usually use the following equation system: mass, momentum and energy conservation equations [22–25]. Solutions of these equations allow us to obtain temperature fields in all projections of a sample to be formed, melt flow rates, cooling rates and crystallization parameters that specify structures and properties of components. At the same time, information on computational temperature fields obtained by using adequate models allows us to predict microstructures and properties of workpieces resulted from different additive manufacturing methods.

The process of manufacturing of components with the use of the additive manufacturing method is followed by complex thermo-mechanical phenomena resulting in the formation of technological residual stresses and possible contraction of components [26–33]. The appearance of internal stresses in an object to be produced is connected with the essential spatiotemporal heterogeneous distribution of temperature and conversion fields.

A standard approach to the numerical solution of temperature deformations and residual stresses in additive manufacturing is to systematically and consistently analyze thermal conductivity in a transient mode and elastoplastic deformations [34]. Further, a transient heat

conduction problem is firstly solved in a numerical manner; then, a temperature field is imported to a mechanical model as “thermal loads” in order to calculate stresses and deformations.

In case of additive technologies with a rather small number of deposition passes, it is acceptable to thoroughly model each pass in the course of production of components [35, 36]. With this modeling method, the supply of heat brought by a thermal source is generally used as a volume thermal flow whose center moves along a deposition trajectory, thereby representing a moving source of heat. However, the additive formation of products usually has a large number of layers, which makes it unreasonable to model each separate pass in the course of creation of components. In order to make calculations more effective, we use a principle where successive melting steps and even layers are grouped together for subsequent simultaneous activation [37, 38]. This method provides that a stationary thermal flow is assigned to a discrete area for a period of time specified by users. It is obvious that the way of building-up of materials and of application of thermal loads in an individual manner is more correct, but requires higher computational efforts.

Therefore, the possibility of modeling of technological processes related to the layer-by-layer synthesis of products by multi-layer deposition of wire materials is a considerable reserve for the purposes of optimizing technological modes of production of components, developing control programs, minimizing defects and increasing manufacturing quality. At the same time, a lot of works are aimed at modeling selective laser melting or laser gas powder deposition welding processes. The modeling of arc methods of deposition welding of wire materials has specific features connected with a large volume of materials to be deposited and, as a result, with great possible deformations of products, as well as with specific aspects of the description of a thermal source [39].

General variable parameters for mathematical models of heat and mass transfer processes with deposition welding with wire materials are as follows:

1. distribution of density of an energy flow of a heat source;
2. initial temperature of a sample;
3. distribution of an additional volume source (in case of additional induction heating);
4. dependence of thermophysical characteristics of materials on temperature;
5. characteristics of phase transitions;
6. velocity of a heat source;
7. orientation and feed rate of wire and its diameter.

As a part of the mathematical models described below, the following assumptions have been accepted:

1. In the process in question, the strength of a plasma arc, the feed rates of a support material  $V_H$  and wire  $V_{II}$  are constant or time intervals of their change considerably exceed a typical time of relaxation of temperature, velocity and concentration fields.

2. The ambient temperature is constant.
3. An energy source is characterized by Gaussian distribution of a thermal flow onto surfaces of a support material and a bed to be deposited.
4. Support and wire materials have the same chemical composition.
5. Molten metal is considered to be an incompressible Newtonian liquid whose physical parameters (density, viscosity, thermal conductivity, etc.) do not depend on temperature.
6. When describing thermal effects in the course of melting and hardening of materials, effective thermal capacity within a quasi-equilibrium model is used.
7. In order to describe the influence of a two-phase zone on the motion of a melt, Darcy term, representing the damping force when fluid passes through a porous media dendrite structures, is introduced to the motion equation [41].
8. An impact on the motion of a melt of electric and magnetic fields generated by a plasma flow is not considered.

Filler wires are fed into the zone of influence of a plasma arc, thereby causing a mass inflow. A plasma arc causes melting and evaporation of a filler material and a base material. The surface of a melt can be somehow deformed under the influence of the arc pressure, of falling droplets (when melting a wire) or of a local increase in metal vapors pressure.

Technological process parameters affect the nature of a metal transfer to a melt. We can distinguish three typical modes:

1. Continuous metal transfer (**Figure 1a**). This mode is carried out at a low strength of a thermal source and is rather low-temperature. This mode slightly changes sizes and a

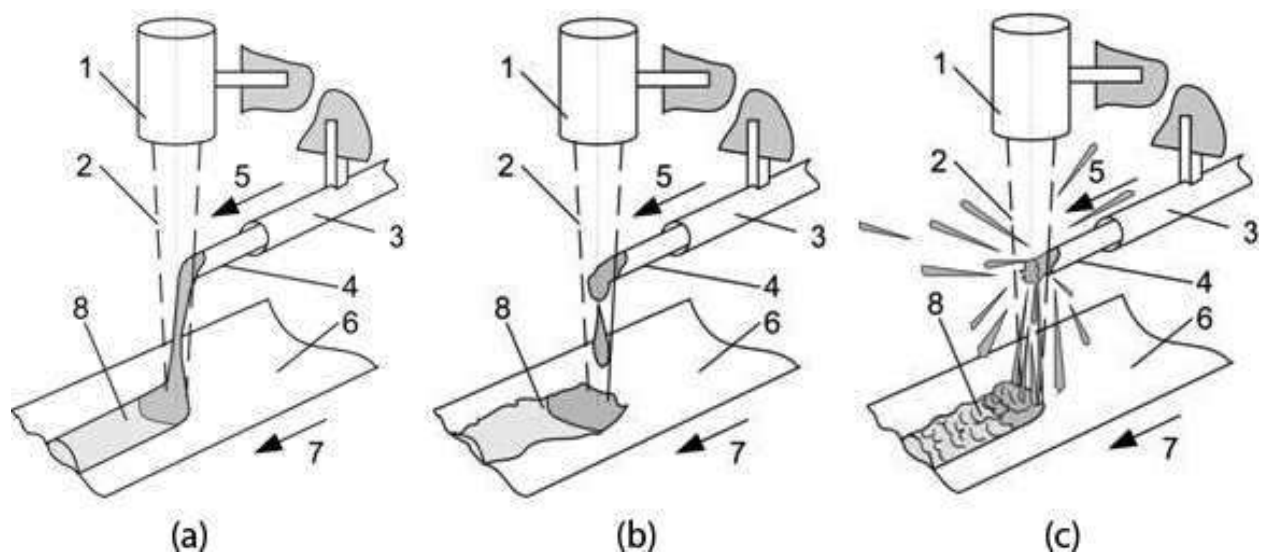


**Figure 1.** Schematically illustrated modes of a mass transfer of a filler material to a melt [40]. *a*—Continuous metal transfer, *b*—coarse-droplet transfer and *c*—spray transfer. 1—Plasmotron; 2—plasma arc; 3—feeder; 4—wire; 5—wire feed direction; 6—product; 7—product motion direction; 8—weld bed being formed.

form of cross section of a weld bed, as well as a structure and physical and mechanical properties of a metal to be deposited. This regime is optimal for the additive process. But their change may be caused only by disturbing factors (instable strength and position of a thermal source, deviation of a wire feed rate or displacement of a product, as well as influence of reheating zones). These factors are not considered at the current stage of works. A further decrease in energy to be delivered results in the fact that wires are melted only partially. This gives rise to formation defects and, therefore, this mode is not satisfactory.

2. A coarse-droplet transfer (**Figure 1b**) takes place when strength is increased above some critical value. The form of a weld bed and its cross dimensions range in length, metal splashes are present, and a crystallization process cannot be considered as a stationary one. This transfer mode may be acceptable for the consumable electrode welding technology. However, its use in most cases results in decreased quality when additive shape-forming processes are implemented.
3. A spray transfer (**Figure 1c**) is carried out in a mode with a higher energy of a thermal source. Metals being constantly fed experience a thermal influence sufficient for strong boiling. This mode is characterized by high spraying and uneven surfaces of weld beds to be formed.

## 2. Mathematical statements of problems (models) of a heat and mass transfer in the course of additive formation of products by melting of wire materials with a plasma arc

The geometry of a computational domain of the model in question is presented in a three-dimensional arrangement (**Figure 2**) and in the X-Z section (**Figure 3**). A surface source of a mass to be deposited onto a solid support material is fed to an interface at the velocity of  $V_{\Pi}$  with some distribution in the X, Y plane (in case of a droplet transfer approximation is possible by Gaussian distribution). A thermal flow from an energy source is determined by Gaussian normal distribution. A minimum temperature in a source is supposed to be higher than the solidus temperature (TS). A mass source moves along a solid support material at the velocity of  $V_H$  (deposition welding velocity). There is the air above a solid support material.

This problem is supposed to be tackled by the shock-capturing method where motion and temperature distribution equations are solved within the whole domain presented in **Figure 2**. In order to describe the motion of a material interface, the level set method is used. The position of an interface and values of material parameters of media (density, viscosity, thermal conductivity, thermal capacity) are determined according to a value of a special remote function  $\phi$ , to which a separate equation is assigned. The level set method helps to determine an interface position between a metal (a molten metal) and the air. The position of a boundary of a phase transition between a solid metal and a melt is established according to a position of an isotherm corresponding to a melting temperature.

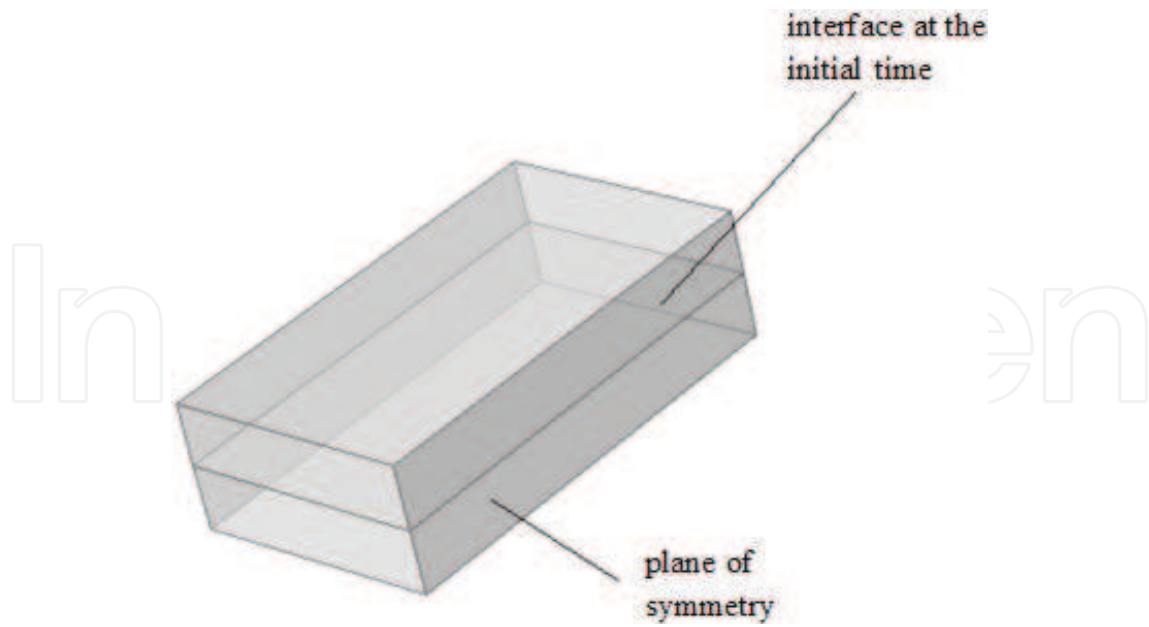


Figure 2. Geometry of the computational domain.

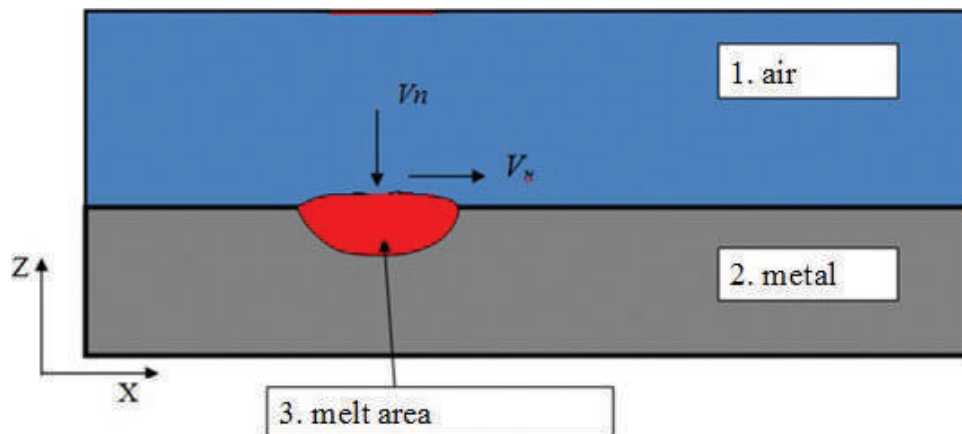


Figure 3. Symmetric longitudinal section of the computational domain.

Courses in metal and in air are described by free thermal convection equations for incompressible media in Boussinesq approximation [42]:

$$\begin{aligned} \frac{\partial}{\partial t} (\rho \vec{u}) + (\vec{u} \nabla) (\rho \vec{u}) &= -\nabla P + \text{Div} \vec{\tau} + \vec{F} \\ \text{div} \vec{u} &= 0 \\ \tau_{ij} &= \mu \left( \frac{\partial u_i}{\partial x_j} + \frac{\partial u_j}{\partial x_i} \right). \end{aligned} \quad (1)$$

where  $\rho$ —density,  $\vec{u}$ —melt flow velocity vector,  $\mu$ —dynamic viscosity,  $P$ —pressure,  $\vec{F}$ —total volume force being as follows:

$$\vec{F} = \rho \vec{g} \beta (T - T_{ref}) - C \left( \frac{1 - f_L}{f_L^3 + B} \right) \vec{u} + \vec{F}_{sv}, \quad (2)$$

where  $g$ —gravitational acceleration,  $\beta$ —thermal-expansion coefficient,  $T$ —absolute temperature,  $T_{ref}$ —initial temperature taken as the solidus temperature ( $T_S$ ).

The first equation member (2) represents thermo-gravitational convection, the second one does energy dissipation of in a two-phase zone (in the zone of a phase transition from a melt to a solid metal), according to the Kozeny-Carman equation where  $B$ —a small computational constant used to avoid division by zero,  $C$ —a constant reflecting the morphology of a two-phase zone (in these studies it is possible to use values around  $10^4 \dots 10^6$ ),  $f_L$ —a function determining the position of a boundary between a liquid phase and a solid one in a metal (fusion zone boundary) [39]:

$$f_L = \begin{cases} 1 & T > T_L \\ (T - T_S)/(T_L - T_S) & T_S \leq T \leq T_L \\ 0 & T < T_S \end{cases} \quad (3)$$

where  $T_L$  and  $T_S$ —liquidus temperature and solidus temperature.

The third equation member (2)  $\vec{F}_{sv}$  is a volume approximation of forces acting at the boundary of a phase interface.

The thermal energy distribution in the computational domain is described by means of the differential energy transfer equation:

$$\frac{\partial T}{\partial t} + (\vec{u} \nabla) T = a \cdot \left( \frac{\partial^2 T}{\partial x^2} + \frac{\partial^2 T}{\partial y^2} + \frac{\partial^2 T}{\partial z^2} \right) + \frac{Q}{c\rho} \quad (4)$$

where  $T$ —absolute temperature,  $a = \lambda/C_{eff} \cdot \rho$ —thermal diffusivity coefficient,  $u$ —melt flow rate,  $c$ —thermal capacity,  $\rho$ —density.

The approach in question provides that the location of a welding source of heat and a source of mass at the “metal-gas environment” interface are arbitrary functions of time. Besides, it is necessary to consider that a wire material is fed to the “metal-gas environment” interface in an already melted state, which also requires some part of energy [43]. In an approximation that the temperature of a melted wire material to be fed is equal to the temperature of a melt at the interface, thermal capacity  $Q$  to be brought in the Eq. (4) is expressed as follows:

$$Q = \left( q_r - q_p - q_h(T - T_0) - \sigma_{c\delta} \varepsilon_u (T^4 - T_0^4) \right) \delta(\phi) n_z, \\ q_r = \eta_0 \frac{2Q_0}{\pi r^2} \exp \left( \frac{-2 \left( (x - V_h t)^2 + y^2 \right)}{r^2} \right) \quad (5)$$

$$q_p = \begin{cases} F_p \rho_L [C_{pS}(T_L - T_0) + L_m + C_{pL}(T - T_L)], & T > T_L \\ F_p \rho_L [C_{pS}(T_L - T_0) + L_m f_L - (1 - f_L)L_m], & T_S \leq T \leq T_L \\ F_p \rho_S [C_{pS}(T - T_0) - L_m - C_{pS}(T_S - T)], & T < T_S \end{cases}$$

$$F_p = N_S(r)V_n$$

where  $Q_0$ —maximum thermal power in a source,  $r$ —radius of a thermal spot from a source,  $\eta_0$ —efficiency of a heat source,  $q_h$ —thermal flow coefficient determined by a convective current,  $\sigma_{cs}$ —Stefan-Boltzmann constant,  $\varepsilon_u$ —metal blackness degree,  $\rho_L$  and  $\rho_S$ —densities of a liquid phase and a solid one of a metal,  $C_{pL}$  and  $C_{pS}$ —specific thermal capacities at a constant pressure of a liquid phase and a solid one of a metal,  $L_m$ —specific metal melting heat,  $N_S(r)$ —function determining the distribution of a material to be delivered to a deposition zone, to be determined by deposition conditions (see **Figure 3**),  $\delta(\phi)$  and  $n_z$ —delta function and normal projection to the boundary of the metal-air interface in the direction of the Z axis setting the distribution of heat along the boundary of the metal-air interface, will be determined below as a part of the description of the level set method.

The latent melting and crystallization heat was taken into consideration by introducing the effective thermal capacity:

$$C_{eff} = C_0 + \frac{\exp \left[ -((T - T_{melt}) / (T_L - T_S))^2 \right]}{\sqrt{\pi}(T_L - T_S)} H_f, \quad (6)$$

where  $C_0$ —thermal capacity depending on temperature,  $H_f$ —latent melting heat,  $T_{melt}$ —melting temperature that is taken as an average one within a range from the solidus temperature to the liquidus one.

When in transition across the boundary of the interface of a liquid phase and a solid one in a metal, viscosity, first of all, suddenly changes from some final value  $\mu_L$  in a melt to an actually infinite value in a solid metal  $\mu_S$ . The value of viscosity in (2) was determined by means of function (4) as [44]:

$$\mu = \mu_L f_L + \mu_S (1 - f_L) \quad (7)$$

In calculations,  $\mu_S$  will be final, but it will be such as  $\mu_S \gg \mu_L$ , which will ensure the “freezing” of a liquid in a solid phase. Sudden changes in density, thermal diffusivity and thermal metal capacity when in transition across the boundary of a phase transition may be described in a similar way.

Surface forces are approximated as volume ones so that:

- volume force  $F_{sv}$  is concentrated in a narrow transitional layer where density and viscosity gradients markedly differ from zero;
- direction  $F_{sv}$  coincides with the direction of remote function gradient  $\phi$ ;
- value  $F_{sv}$  is proportional to the gradient of a remote function and the curvature of a surface;

- in a limiting case, when a transitional layer turns into a jump in typical parameters of a liquid, the consideration of this volume force leads to an ordinary dynamic condition on the surface of an interface.

Based on the mentioned assumptions, an expression for the volume force is written as:

$$\vec{F}_{sv} = - \left( \sigma k(\phi) \nabla \phi - \frac{\partial \sigma}{\partial T} \nabla_s T - p_\delta \vec{n} \right) \delta(\phi) \quad (8)$$

where  $\phi$ —marker function,  $k(\phi)$ —interface surface curvature,

$$k(\phi) = \operatorname{div} \vec{n}, \quad \vec{n} = \frac{\nabla \phi}{|\nabla \phi|}, \quad n_z = \frac{1}{|\nabla \phi|} \frac{\partial \phi}{\partial z} \quad (9)$$

$\delta(\phi)$ —Dirac delta function,  $\sigma$ —melt surface tension coefficient.

The first addend in (8) describes capillary forces acting normally to the surface of the metal-air interface, the second addend describes thermo-capillary Marangoni forces acting tangentially to the surface where  $\nabla_s T$ —temperature gradient component tangential to a curved surface. The third addend specifies the pressure force of plasma arc [44]:

$$p_\delta = 2k_I I_a \exp \left( \frac{-2 \left( (x - V_{ht})^2 + y^2 \right)}{r^2} \right) \quad (10)$$

where  $I_a$ —arc current,  $k_I$ —electrodynamical constant.

In the level set method, the position of an interface boundary is determined by a zero value of a level set or remote function  $\phi$ . As for the remote function, we solve a transfer equation that will be as follows:

$$\frac{\partial \phi}{\partial t} + \left( F_p + \vec{n} \cdot \vec{u} \right) \cdot |\nabla \phi| = 0 \quad (11)$$

Density, viscosity or concentration values are restored according to the remote function. For example, in case of density we have:

$$\rho(\phi) = \rho_1 + (\rho_2 - \rho_1) H(\phi) \quad (12)$$

where  $\rho_1$  и  $\rho_2$ —media density,  $H(\phi)$ —Heaviside function set by the following expression:

$$H(\phi) = \begin{cases} 0 & \text{if } \phi < 0, & \text{air} \\ \frac{1}{2} & \text{if } \phi = 0 \\ 1 & \text{if } \phi > 0, & \text{metall} \end{cases} \quad (13)$$

For numerical implementation, expression (13) is written as

$$H_\varepsilon(\phi) = \begin{cases} 0 & \text{if } \phi < -\varepsilon \\ \frac{1}{2} \left[ 1 + \frac{\phi}{\pi} - \frac{1}{\pi} \sin(\pi\phi/\varepsilon) \right] & \text{if } |\phi| \leq \varepsilon \\ 1 & \text{if } \phi > \varepsilon \end{cases} \quad (14)$$

The delta function in expressions (5) and (8) is equal to

$$\delta(\phi) = H'_\varepsilon(\phi) = \frac{\partial}{\partial \phi} H_\varepsilon(\phi) \quad (15)$$

$$\delta(\phi) = \begin{cases} \frac{1}{2\varepsilon} \left[ 1 + \cos\left(\frac{\pi\phi}{\varepsilon}\right) \right] & \text{if } |\phi| \leq \varepsilon \\ 0 & \text{otherwise} \end{cases} \quad (16)$$

The thickness of a transitional layer between the phases is equal to  $2\varepsilon$ . It is usually supposed that  $\varepsilon = \alpha\Delta x$  where  $\Delta x$  is a distance between nodes of a spatial grid or a grid cell size around a boundary,  $\alpha$  is an integer.

Far from a fusion zone, at all boundaries of the computational domain, except for an upper boundary, a media velocity is supposed to be equal to zero. At the upper boundary, pressure is supposed to be set. For the remote function, at all boundaries the normal derivative is supposed to be equal to zero. Thermal conditions at the boundaries of the computational domain are determined by external technological conditions, but for model calculations all boundaries may be considered to be thermally insulated.

### 3. Description of a thermal source when using a plasma arc at various polarity

When modeling heat and mass transfer processes with the use of a plasma arc as a thermal source, there is a factor concerning the description of a thermal source, especially when using a plasma arc with current reverse polarity. A heat transfer to a product, under the influence of a plasma direct arc, is carried out by two mechanisms: convection from a plasma spray (a plasma flow) and heat emission in discharge (electrode) spots. Work [45] establishes that at an identical current and under all other conditions being equal a heat input to a product, during the operation of a plasmatron with current reverse polarity, is 1.3... 1.6 times higher than with current direct polarity, which is explained by a higher arc voltage. Unlike a constricted arc of direct polarity, a constricted arc of reverse polarity is characterized by a thermal power distributed more uniformly along the surface of a product (Figure 4).

It should be noted that at plasma processing with a current of direct polarity values  $d_{pf}$  and  $d_{as}$  are proportional, and it is impossible to control their size separately. The diameter of a plasma flow  $d_{pf}$  is actually determined by the diameter of a nozzle  $d_{pf} \approx d_n$  [46]. The distribution of density of a full thermal flow at direct polarity deposition welding is described by Gaussian distribution.

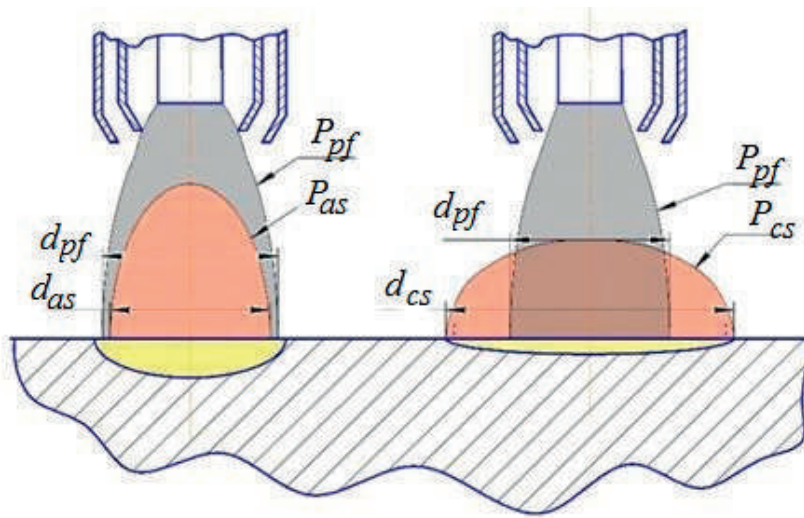


**Figure 4.** Chart of a heat transfer to a product at plasma processing. a—Current direct polarity, b—current reverse polarity.  $P_{pf}$ —Power delivered by convection by a plasma flow,  $P_{as}$ —power emitted at an anode spot,  $P_{cs}$ —power emitted in a cathode region,  $d_{pf}$ —diameter of a plasma flow,  $d_{as}$ —diameter of an anode spot,  $d_{cs}$ —diameter of a cathode region.

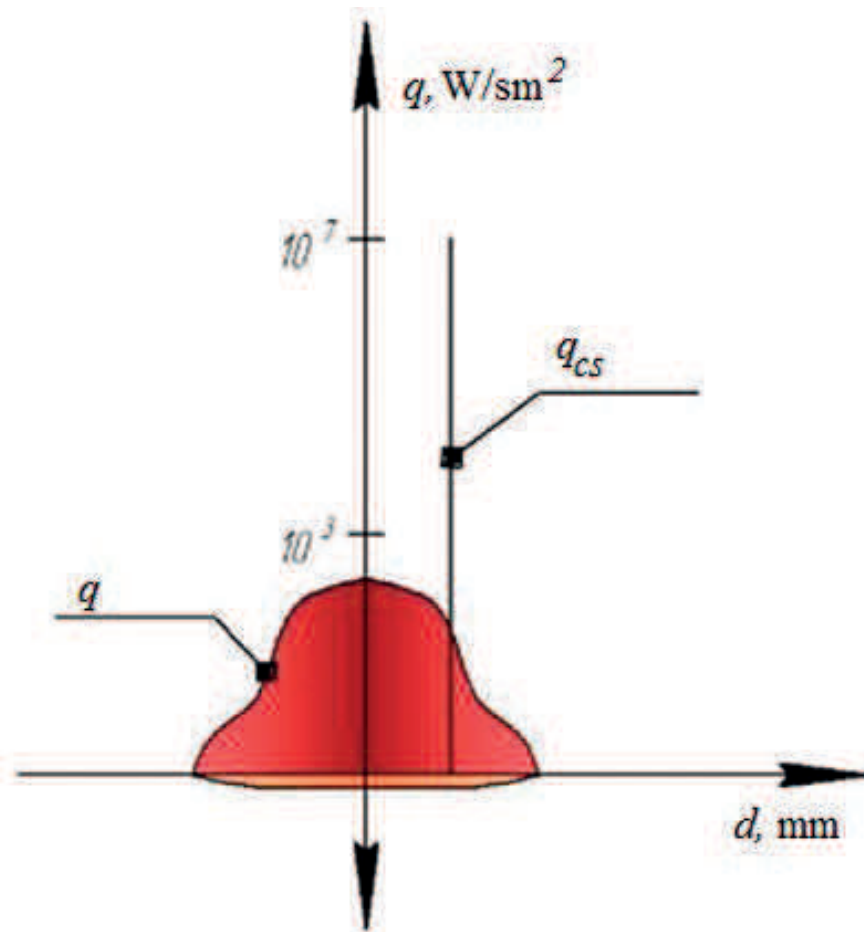


**Figure 5.** Aspects of a heat transfer to a product during the operation of a plasmotron with a current of reverse polarity.  $q_{cs}$ —Density of a thermal flow from a non-stationary cathode spot,  $q$ —density of a resulting thermal flow,  $d$ —diameter of the influence of a thermal flow,  $h$ —fusion depth of a base.

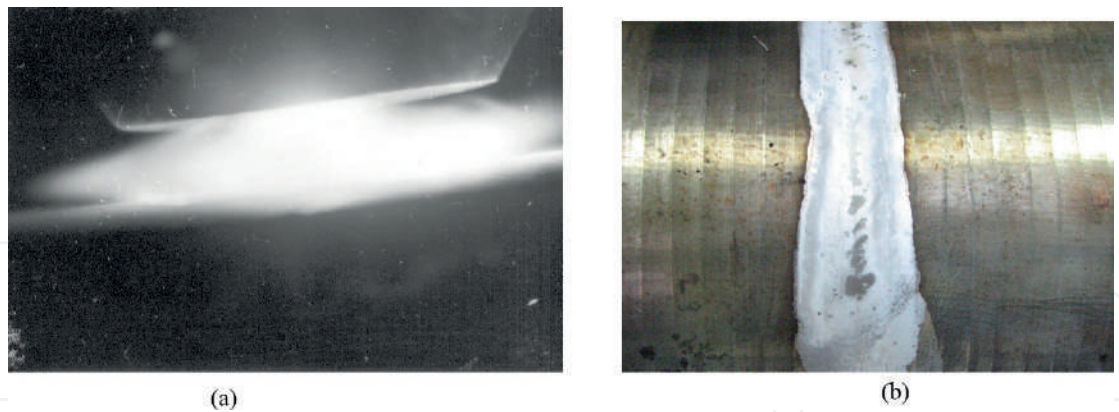


**Figure 6.** Traveling of cathode spots along a product surface during the operation of a reverse polarity plasmatron.

With current reverse polarity, a plasma arc belongs to a type of arcs with non-stationary cathode spots traveling along the surface of a cathode. A travel width depends on the design of a plasmatron and the material of a product. One of distinctive features of non-stationary spots is their short-term existence and high current density ( $j \sim 10^5 - 10^6 \text{ A/m}^2$ ), and local specific thermal flows in the area of short-term influence at a spot reach values ( $q \sim 10^6 - 10^7 \text{ W/cm}^2$ ) (Figure 5). The time-averaged thermal influence of cathode spots can be approximated evenly by a thermal source distributed along the area restricted to  $d_{cs}$ . The distribution of density of a thermal flow delivered by a plasma flow at reverse polarity deposition welding is described by Gaussian distribution. The diameter of a plasma flow  $d_{pf}$  is supposed to be the diameter of a nozzle  $d_{cs} \approx d_n$  [46]. For the deposition of metal during the layer-wise formation, the following equipment which has been developed at Perm National Research Polytechnic University was used: the plasma welding unit BPS-350; universal plasmatron PM1-15.

A value  $d_{cs}$  under the influence of an arc with current reverse polarity, can be actively controlled.

The size of a cathode region depends on parameters of a technological mode and requires determination. The travel of cathode spots leads to a known phenomenon of cathode cleaning under the influence of an electric arc of reverse polarity [47] on the surface of metals. It is generally believed [48] that the destruction and removal of an oxide film from a product surface in the area of influence of a reverse polarity arc result from attacking the surface of a metal by positive ions.

When a plasmatron operates with a reverse polarity current on a surface subjected to cathode cleaning, there is a visible mark [49] that allows us to visually estimate the area of traveling of cathode spots (Figure 6).

A phenomenon of cathode cleaning can be used to create a statistical dependence of the influence of technological parameters of reverse polarity plasma arcs on the diameter of a cathode region. At the first stage, it is possible to use an empirical model [48].

$$d_{cs} = 7,918 + 0,108I_a + 1,235Q_p + 1,235Q_{pg} - 0,238V - 0,599H, \quad (17)$$

where  $I_a$ —arc current,  $Q_{pg}$ —protective gas consumption (l/min),  $Q_p$ —plasma-forming gas consumption (l/min),  $V$ —plasmatron displacement speed, m/h,  $H$ —plasmatron nozzle height above a product (mm).

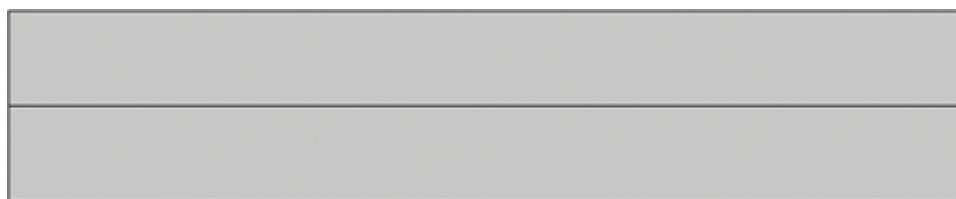


**Figure 7.** Geometry of the computational domain.

Therefore, a plasma source at reverse polarity deposition welding is represented by a combination of a source of heat delivered by a plasma flow with Gaussian distribution, of diameter  $d_{pf}$ , and an evenly distributed source of diameter  $d_{cs}$ . An energy ratio between these sources is determined experimentally according to the method suggested in the work [50].

In order to analyze the applicability of selected approaches, the preliminary numerical implementation in the two-dimensional statement of a problem of melting of wire materials with concentrated and arc energy sources was carried out. A Comsol 4.4 application software package (Heat Transfer, Level Set and Laminar Flow modules) was used. The geometry of the computational domain is presented in **Figure 7**.

The sizes of the computational domain are 50 mm (length) and 10 mm (height). A process simulation area was covered with a two-dimensional grid included in the computational domain. The grid had an even pitch. The size of a cell was 0.3 mm.

A 304-L stainless steel was accepted as a model material. The stainless steel workpiece had a composition of 18.2% Cr, 8.16% Ni, 1.71% Mn, 0.02% C, 0.082% N, 0.47% Mo, 0.44% Si, 0.14% Co, 0.35% Cu, 0.0004% S, 0.03% P, and balance Fe. Many thermophysical characteristics of materials are functions of temperature [51–54]. At this stage, these nonlinearities were not taken into consideration. **Table 1** specifies accepted values that were used in calculations. Parameters of the deposition welding mode presented in **Table 2**. As boundary conditions for a model example all boundaries, except for a lower one, were taken as thermally insulated. At the lower boundary, a constant temperature of 273 K was maintained.

**Figure 8** shows the distribution of temperature in a sample to be deposited 2 s later after the beginning of a process. A melt area is marked by a line.

Attribute	Designation	Size	Value
Liquidus temperature	$T_S$	[K]	1723
Solidus temperature	$T_L$	[K]	1673
Specific heat capacity	$C$	[J·kg <sup>-1</sup> ·K <sup>-1</sup> ]	500
Density	$\rho$	[kg·m <sup>-3</sup> ]	7000
Thermal conductivity	$\lambda$	[W·m <sup>-1</sup> ·K <sup>-1</sup> ]	28.9
Specific melting heat	$H_f$	kJ/kg	84

**Table 1.** Thermophysical characteristics of materials used in calculations [51–54].

Source strength, W	Source displacement velocity, mm/s	Wire feed rate, mm/s
800	5	15

**Table 2.** Deposition mode parameters.

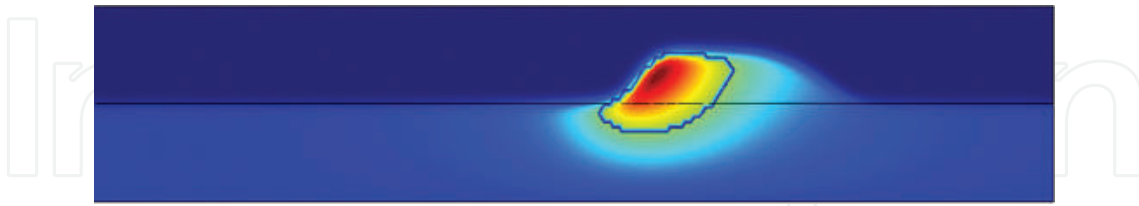


**Figure 8.** Distribution of temperature in the course of deposition welding.

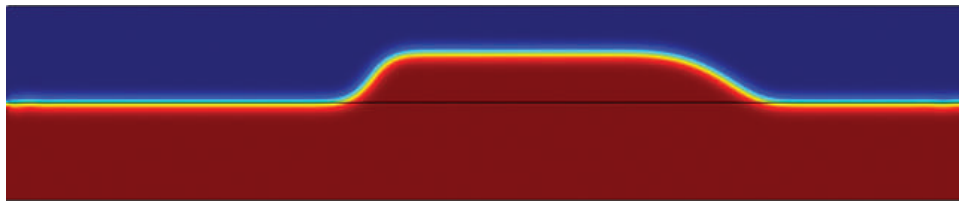


**Figure 9.** Weld bed formation results.

The deposition welding results obtained upon completion of a 4-s process are given in [Figure 9](#). This model appropriately helps to determine distributions of temperatures, melt flow rates, pressures, components of heat flow densities, forms and sizes of weld beds to be deposited.

#### **4. Development of the models intended to form fields of residual stresses and deformations in products resulted in the course of additive formation by melting wire materials with a plasma arc**

The process of manufacturing of components with the use of the additive manufacturing method is followed by complex thermo-mechanical phenomena resulting in the formation of technological residual stresses and possible contraction of components [28, 30–32, 55–58]. The appearance of internal stresses in an object to be produced is connected with the essential spatiotemporal heterogeneous distribution of temperature and conversion fields. The appearance of residual stresses is caused due to the fact that inelastic deformations [33] are not consistent, first of all, temperature shrinkage deformations at cooling, structural shrinkage due to the course of phase transformations (melt crystallization) that is notable for a deformation history of various material points because of heterogeneous temperatures, temperature gradients and temperature velocities.

In most cases, such measures as preliminary natural validations of technologies, selection of certain locations of components, selection of technological modes, are taken in order to

eliminate and minimize any geometrical defects arising in the course of manufacturing of modern components, which is a serious obstacle to organizing comprehensive digital manufacturing processes.

An approach associated with creating and using mathematical and computer models of thermomechanical behaviors of components in the course of additive manufacturing allows us not to carry out natural experiments at a stage of design of technological process parameters and structural parameters and to predict qualitative and quantitative characteristics of stress conditions and contractions of future components, as well as study the effectiveness of possible measures aimed at decreasing residual stresses and deformations (heat treatment).

Calculation of residual stresses and warpage for the wire fusion process remains the most difficult aspect in numerical simulation. Often, the addition of material is modeled by adding and (or) activating new elements to previously placed ones. The growth of new elements adds additional rigidity to the existing structure and requires the gradual addition of more and more new elements to the solution area. There are three most commonly used methods of modeling material deposition—the so-called birth element (1), a quiet element (2) and hybrid activation (3) [59, 60]. In the method of the birth element, the elements for the material that has not yet been created are deactivated (and thus not included in the solution area), and then gradually regenerated and included in the solution area. In the method of sleeping elements, all elements are present in the calculation model from the very beginning and have artificial properties with very low rigidity. As the details grow, the properties of these elements gradually switch to real physical properties. Finally, the hybrid activation method combines the methods of emerging and sleeping elements, where only the current deposition layer is activated and set to a sleeping state, and all subsequent layers are deactivated [60].

For products with a relatively small number of surfacing passages, detailed modeling of each passage in the construction of a part is permissible [35, 36]. With this method of modeling, the heat input from the beam energy is usually applied as a volumetric heat flux whose center moves along the trajectory of surfacing, thus representing a moving heat source. Such a method with a moving heat source was used to model both Directed Energy Deposition (DED) [36] and Powder Bed Fusion (PBF) [35] additive production processes. Nevertheless, usually the product has a large number of layers, which makes it impractical to simulate each individual passage when creating a part. To ensure greater efficiency of calculations, the principle is used, in which the successive melting steps and even the layers are grouped together for subsequent simultaneous activation [37, 38].

We know studies aimed at modeling additive manufacturing processes, optimizing thermal cycles, estimating the influence of process parameters on changes in forms of finished products [59–80].

A large volume of research has been published for PBF from various materials, ranging from stainless steel [19, 63–65], carbon steels [78–80], nickel alloys [69–75] and titanium alloy Ti-6Al-4V [34, 69–72, 75, 76]. By modeling residual stresses and deformations for additive technologies using wire, much less work has been published than for powder systems. The normalized maximum residual stress is presented in [19, 64] as a function of the power, scanning speed,

and preheating of the substrate in the construction of a thin-walled structure. In [64] 3D sequential temperature and elastic calculations were performed using the COMSOL and MATLAB packages. In [65], a 3D sequential temperature and elastic-plastic analysis was performed in the SYSWELD package. In works [66, 67] the ABAQUS is used for sequential temperature and elastic-plastic 3D analysis, deformation due to a phase transition is taken into account. In [62, 73], the COMET program and element activation technology are used, a thermo-elasto-viscoplastic material model is used. Additive technology Wire Arc Additive Manufacturing (WAAM) is suitable for manufacturing parts that require a large amount of surfacing [69, 72, 77]. In [69–72] for WAAM technology in ABAQUS software, 3D analysis is performed, assuming the elastic-plastic behavior of the material.

To improve the efficiency of the calculations, Li et al. [78] proposed a method that displays the local residual stress field calculated at the mesoscale level for the rapid prediction of warping of a part. Another approach to efficient modeling warping is to use the inherent-strain method, developed by Yuan and Ueda to calculate the deformation in welding large-sized parts [79]. The method directly applies a known proper (initial) deformation to calculate buckling and does not require a numerical solution of non-stationary temperature and elastoplastic problems in a step-by-step formulation. Finally, Mukherjee et al. [71, 75] constructed an analytical expression for the special deformation parameter for estimating the maximum residual strains as a function of the linear heat release, substrate stiffness, maximum temperature, the thermal expansion coefficient of the fusion alloy and the Fourier number, which expresses the ratio between the speed changes in the thermal conditions in the environment and the speed of the adjustment of the temperature field inside the system under consideration.

The numerical modeling of residual stresses and thermoshrinkable deformations at additive formation of products with the use of wire materials melted by a plasma arc is considered below.

In view of small deformations and negligibly small dissipative heat emission, it is possible to divide a boundary problem of non-stationary thermal conductivity and a boundary problem of thermomechanics with regard to a stressed-deformed state that are unrelated in such statement. Death and birth technologies (Elements Birth and Death in ANSYS) with regard to material parts (originally absent in a model and then added in the course of deposition) can be used in order to solve them. At the same time, an area occupied by an already finished product is considered as a computational one. The continuous building-up of a material is carried out discretely, at each substage of calculation corresponding to the “birth” of a next subarea from “dead” elements, a boundary problem of heat conductivity and thermomechanics is solved, and a result of solution of a previous substage serves as initial conditions for a subsequent one.

At substage  $k$ , the statement of a boundary problem of non-stationary heat conductivity according to temperatures fields  $T(\mathbf{x}, t)$  in area  $V_k$  with boundary  $S_k$ , with accepted hypotheses taken into consideration, includes [81]:

Thermal conductivity equation:

$$\rho(\mathbf{x})c(\mathbf{x}, T) \frac{\partial T}{\partial t} = \operatorname{div}(\lambda(\mathbf{x}, T)\operatorname{grad}(T)) + \rho(\mathbf{x})\dot{q}(\mathbf{x}, t), \mathbf{x} \in V_k \quad (18)$$

where  $c(\mathbf{x}, T)$ ,  $\lambda(\mathbf{x}, T)$ ,  $\rho(\mathbf{x})$ —thermal capacity, thermal conductivity and density of an unevenly alloyed material,  $\dot{q}(\mathbf{x}, t)$ —specific strength of an external heat source.

Boundary conditions:

$$-\lambda(\mathbf{x}, T) \text{grad}(T) \cdot \mathbf{n} = h(T) \cdot (T - T_c(t)) + \varepsilon \sigma_0 (T)^4 + \int_{S_k} \frac{I_e}{r^2} \cos \theta dS_k, \quad \mathbf{x} \in S_k \quad (19)$$

where the first addend of a right part describes a convective heat transfer, and the second one—radiation (the Stefan-Boltzmann law); the third one—radiation from a plasmatron nozzle,  $\varepsilon$ —blackness coefficient,  $\sigma_0$ —Stefan-Boltzmann constant,  $I_e$ —source radiation capacity,  $r$ —distance between a surface point and a source, and  $\theta$ —angle that is formed by a surface normal directed to a source,  $h(T)$ —heat transfer coefficient,  $T_c(t)$ —ambient temperature,  $\mathbf{n}$ —external single normal to the boundary  $S$  of a body being cooled.

Initial conditions:

$$T(\mathbf{x}, t_{0,k}) = T_{k-1}(\mathbf{x}), \quad \mathbf{x} \in V_k \quad (20)$$

where  $T(\mathbf{x}, t_{0,k})$ —initial temperature distribution for substage  $k$ ,  $T_{k-1}(\mathbf{x})$ —temperature determined at the end of a previous one.

These relations consider that an area of study  $V_k = V_k^{liv} \cup V_k^{kil}$  remains invariable throughout a substage. Here  $V_k^{liv}$  and  $V_k^{kil}$  are used to mark zones occupied by “live” and “dead” elements respectively. At the same time, thermophysical properties of the material in the area of “dead” elements are subject to degradation:

$$\begin{aligned} c(\mathbf{x}), \mathbf{x} \in V_k^{kil} &<< c(\mathbf{x}, T), \mathbf{x} \in V_k^{liv}, & \rho(\mathbf{x}), \mathbf{x} \in V_k^{kil} &<< \rho(\mathbf{x}, T), \mathbf{x} \in V_k^{liv}, \\ \lambda(\mathbf{x}), \mathbf{x} \in V_k^{kil} &>> \lambda(\mathbf{x}, T), \mathbf{x} \in V_k^{liv}. \end{aligned}$$

An unrelated quasistatic boundary problem of mechanics of a deformable solid body, taking into account the insignificance of a contribution of mass forces at substage  $k$ , includes [82, 83]:

Equilibrium equations:

$$\text{div } \hat{\sigma} = 0, \quad \mathbf{x} \in V_k \quad (21)$$

where  $\hat{\sigma}(\mathbf{x}, t)$ —stress tensor;

Cauchy geometrical relations:

$$\hat{\varepsilon} = \frac{1}{2} \left( \nabla \mathbf{u} + (\nabla \mathbf{u})^T \right), \quad \mathbf{x} \in V_k \quad (22)$$

where  $\mathbf{u}(\mathbf{x}, t)$ —displacement vector,  $\hat{\varepsilon}(\mathbf{x}, t)$ —total deformation tensor.

Displacement boundary conditions:

$$\mathbf{u} = \mathbf{U}, \quad \mathbf{x} \in S_{u,k} \quad (23)$$

Stress boundary conditions:

$$\hat{\sigma} \cdot \mathbf{n} = \mathbf{P}, \mathbf{x} \in S_{\sigma,k} \quad (24)$$

where  $S_u, S_\sigma$  — parts of a boundary border with set displacements and loads respectively.

Thermomechanical properties of the material in the area of “dead” elements exclude physical nonlinearity and are perfectly elastic with degraded values:

$${}^4\hat{C}(\mathbf{x}), \mathbf{x} \in V_k^{kil} \ll {}^4\hat{C}(\mathbf{x}, T), \mathbf{x} \in V_k^{liv},$$

where  ${}^4\hat{C}$  — the fourth-rank tensor of elastic constants of the material.

The general equation system of the deformable solid body mechanics boundary value problem includes constitutive relations as well. To describe the viscoelastoplastic behavior of the alloy under study, we used the Anand [84] model included to the list of ANSYS physical models. The model has the following form:

$$\hat{\sigma} = {}^4\hat{C} \cdot \cdot (\hat{\varepsilon} - \hat{\varepsilon}_T - \hat{\varepsilon}_B) \quad (25)$$

$$\hat{\varepsilon}_T(\mathbf{x}, t) = \hat{E} \int_{T_0}^T \alpha(\mathbf{x}, T(\mathbf{x}, t)) dT \quad (26)$$

where  ${}^4\hat{C}$  — the fourth-rank tensor of elastic constants of the material;  $\hat{\varepsilon}_e(\mathbf{x}, t) = \hat{\varepsilon}(\mathbf{x}, t) - \hat{\varepsilon}_T(\mathbf{x}, t) - \hat{\varepsilon}_B(\mathbf{x}, t)$  — the tensor of elastic deformations,  $\hat{\varepsilon}(\mathbf{x}, t)$  — the tensor of total deformations;  $\hat{\varepsilon}_T(\mathbf{x}, t)$  — the tensor of temperature deformations;  $\hat{\varepsilon}_B(\mathbf{x}, t)$  — the tensor of viscous deformations;  $\alpha(\mathbf{x}, T)$  — the coefficient of temperature expansion of the material;  $T_0$  — the onset temperature of temperature deformation;  $\hat{E}$  — the second-rank identity tensor. The viscous deformation rate is calculated according to the formula:

$$\dot{\hat{\varepsilon}}_B(\mathbf{x}, t) = \dot{\varepsilon}_B(\mathbf{x}, t) \left( \frac{3\hat{s}}{2q} \right),$$

where  $\hat{s}(\mathbf{x}, t) = \hat{\sigma}(\mathbf{x}, t) - \sigma(\mathbf{x}, t)\hat{E}$  — the stress deviator;  $\sigma(\mathbf{x}, t) = \sigma_{kk}/3$  — the average stress;  $q$  — the equivalent stress  $q = \sqrt{\frac{3}{2}\hat{s} : \hat{s}}$  (the following symbol “:” means a scalar product, the symbol “..”, set in earlier, means a tensorial product);  $\dot{\varepsilon}_B = \sqrt{\frac{2}{3}\dot{\hat{\varepsilon}}_B : \dot{\hat{\varepsilon}}_B}$  — the equivalent viscous deformation rate connected to the other parameters by the following formula:

$$\dot{\varepsilon}_B = A e^{-\frac{H}{kT}} \left[ \sinh \left( \xi \frac{\sigma}{S} \right) \right]^{\frac{1}{m}} \quad (27)$$

The model also includes the evolutionary equation:

$$\dot{S} = \left\{ h_0 (|B|)^a \frac{B}{|B|} \right\} \dot{\varepsilon}_B \quad (28)$$

The equation involves a possibility of work hardening and work softening. The designations are as follows:

$B = 1 - \frac{S}{S^*}$ ;  $S^* = S_1 \left[ \frac{\dot{\varepsilon}_B}{A} e^{\frac{U}{RT}} \right]^n$ ;  $\sigma$ —the stress intensity;  $S$ —the resistance to deformation (scalar function of hardening);  $S^*$ —the saturation value of the hardening function;  $R$ —the absolute gas constant;  $U$ —the activation energy;  $T$ —the absolute temperature;  $A$ ,  $a$ ,  $m$ ,  $n$ ,  $h_0$ ,  $\xi$ ,  $S_1$ —the empirical coefficients.

Taking into account behavior characteristics of the elements activated according to the technology used at ANSYS, the formulas (25) are transposed to the following form:

$$\hat{\sigma} = {}^4\hat{C} \cdot (\hat{\varepsilon} - \hat{\varepsilon}_T - \hat{\varepsilon}_B - \hat{\varepsilon}_{k-1}) \quad (29)$$

where  $\hat{\varepsilon}_{k-1}$ —the total deformation calculated up to the end of  $k - 1$ -th sub-step (the current status at the moment of activation of the element is its natural state).

As the setup of the mechanical problem (Eqs. (21)–(28)) imply, the ANSYS system of hypotheses does not include separation of the stress tensor into any components. The input of separate factors to the stress field generation is covered by the corresponding deformation types (see the formula (25)). At that, shrinkage due to phase transformation is covered by temperature deformation with the help of corresponding adjustment of the thermal coefficient of linear expansion within the solidus-liquidus interval.

The algorithm of calculations of temperature fields in numerical simulation of the plasma deposition process in the finite element ANSYS package stipulates performance of the following computational procedures:

1. To create the finite element model including volumes to be occupied by the product divided to separate horizontal layers as well as the platform—the basis with suitable thermal and physical properties.
2. To “kill” (the EKILL command) a part of the elements that are not involved in the real process of building up before its beginning.
3. In the cycle of layer building up beginning from the bottom layer:  
To define conditions of convective heat exchange at the upper boundary of the layer according to the formula (19).

In the cycle of sub-steps of passing the deposition areas of the successive computational layer:

To remove a part of the layer at its bottom boundary under the area of previously defined conditions of convective heat exchange where available.

To activate (the EALIVE command) all elements of the  $k$ -th area.

To heat a part of the area's elements distributed around the volume using a thermal energy source (see the formula (18)) for a time of plasma arc impact.  $t_a$ .

To remove the heat source and wait for the holding time  $t_{wi}$ .

4. To wait until the system cools down completely (partially). Solution of a non-stationary problem with known boundary conditions for a thermo-mechanical model, all of whose elements are active.

The impact time of the plasma arc  $t_a$ , taking into account possible overlapping of plasmatron motion paths, is calculated according to the formula

$$t_a = \frac{S_s}{v_s \cdot ds} \quad (30)$$

where  $S_s = \pi D_s^2/4$ —the size of the spot,  $v_s$ —the movement speed of the plasmatron,  $ds$ —the distance between adjacent tracks.

The holding time  $t_{w,k}$  for the  $k$ -th building up area is defined by the following expression:

$$t_{wi} = \frac{S_k}{ds \cdot v_s} \quad (31)$$

where  $S_k$ —the size of the area.

The specific capacity of heat emission on the surface of the heated spot of the deposited material is defined according to the following formula:

$$\tilde{W}_T = K \cdot W/S_s \quad (32)$$

where  $W$ —the capacity of the plasma arc,  $K$ —the heating fraction of the capacity.

The specific volumetric capacity of the heat source used in the Eq. (18) has the following form:

$$\dot{q} = \dot{q}_s \cdot S_k/V_k = \frac{W \cdot K}{S_s \cdot h_k} \quad (33)$$

where  $V_k$ —the volume of the deposited area,  $h_k$ —the thickness of the layer. Thickness of the deposited layer  $h_k$  is defined on the basis of experimentally observed total height of the deposited part of the product and actual number of layers.

The discrete model of the computational domain is similar to the model of the heat conductivity problem above. Before calculation, the Solid279 heat element is replaced with Solid286, which uses displacements as the degrees of freedom, and thermomechanical properties are added. The algorithm is similar to that of Item 4.1.:

1. To “kill” (the EKILL command) a part of the elements that are not involved in the real process of building up before its beginning. To define boundary conditions in displacement (e.g. fixation along the cutting plane, vertical fixation in entrapment zones etc.).
2. In the cycle of layer building up beginning from the bottom layer:

In the cycle of sub-steps of passing the deposition areas of the successive computational layer:

To activate (the EALIVE command) all elements of the  $k$ -th area.

To implement temperatures, previously calculated for that moment of time, to the units of the model for the impact time of the ray  $t_a$ .

To implement temperatures, previously calculated for the end moment of the holding time, and hold for  $t_{wi}$  seconds.

3. To read the temperature field for the period of partially cooldown of the system, to calculate SSS.
4. To implement the ambient temperature, to release the entrapment, to calculate SSS.

After that we performed preliminary verification of the mathematical model and numerical algorithm for solution of the three-dimensional problem of metal products manufacturing using plasma deposition of wire materials. For the reference we took the results of the experiment for wire deposition on a metal base using arc surfacing in shielding gases with a tungsten (nonconsumable) electrode as described in the Article [85]. **Figure 10a** shows the plate in question with the dimensions of 275 x 100 x 12 mm. We build up a metal rib with the length of 165 mm and the cross section showed in **Figure 10b** on the upper surface of the object.

The arc deposition process is performed in 2 steps. The first step involves preliminary heating of the base plate that is performed by torch back and forth movement with the speed of  $v_s = 5$  mm/s and the impacted area that is 1.5 times larger than the base area of the deposited rib. Power consumption of the torch is  $W = 2.7$  kW, diameter of the spot is  $D_s = 6$  mm. Subsequent deposition is performed in 10 layers along a continuous path (the process continues backward).

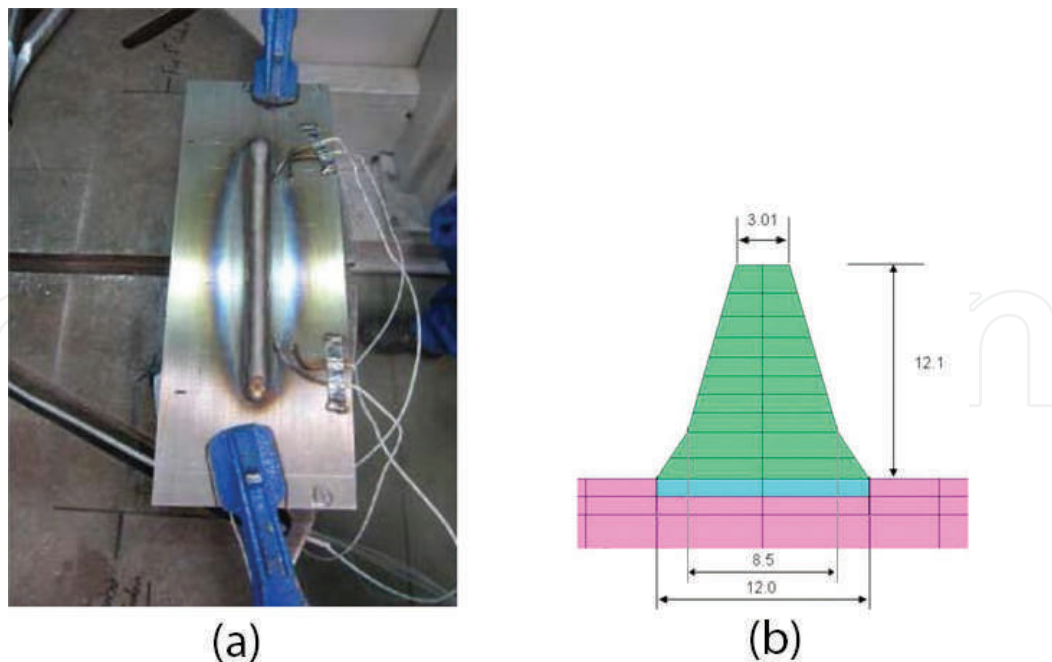


**Figure 10.** Product view illustration after the experiment with fixation and sensor systems (a), dimensions of the deposited area at the cross section, mm (b) [85].

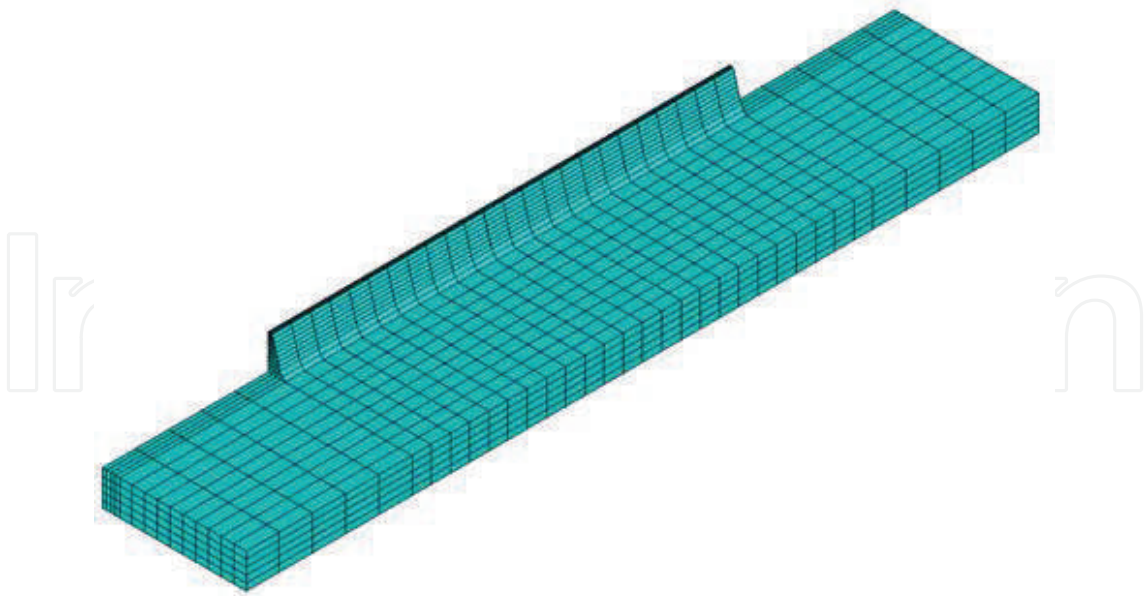


**Figure 11.** The discrete model of the building up problem.

**Figure 11** shows the finite element model of the problem. 20-unit isoparametric Solid 279 elements were used for solution.

The Inconel 718 nickel alloy was used as the material for calculation [86].

Thermal and physical properties of the material were taken from the Article [87]. In addition to the above, according to the data, represented in the Article, the density  $\rho = 8170 \text{ kg/m}^3$  and thermal conductivity  $\lambda = 30 \text{ W/(m K)}$  were deemed as constants. Temperature dependence of the enthalpy  $H(T)$  is presented in **Figure 12**. Heat capacity of the material, included in the thermal conductivity equation, was calculated according to the formula  $c(T) = dH(T)/dT$ . It should be noted that variations at the arc  $H(T)$  in the range of 1500–1600 K in **Figure 12** arise from heat emission during solidification of the alloy. Heating fraction of the plasma arc capacity  $K$  was set to 0.2 for calculation.

Identification of the chosen Anand model (25)–(28) for the material under study was performed according to the data of the stretch experiment with the defined speed at different temperatures represented in the Article [87].

The required constants of the model were defined in several steps by the downhill simplex method in the Matlab package. At that, relative disparity of computational and experimental values of voltage in Diagram  $\sigma - \varepsilon$  (**Figure 13**) was minimized.

As the result, the following values of material constants were obtained by the authors of this publication:

$$S_0 = 2.0447e + 05 \text{ Pa}, U/R = 2.0864e + 03, \xi = 0.3335, A = 2.5008e + 04, m = 0.4363, h_0 = 4.0352e + 06, \\ S_1 = 3.2148e + 07 \text{ Pa}, n = 0.2273, a = 0.4461.$$

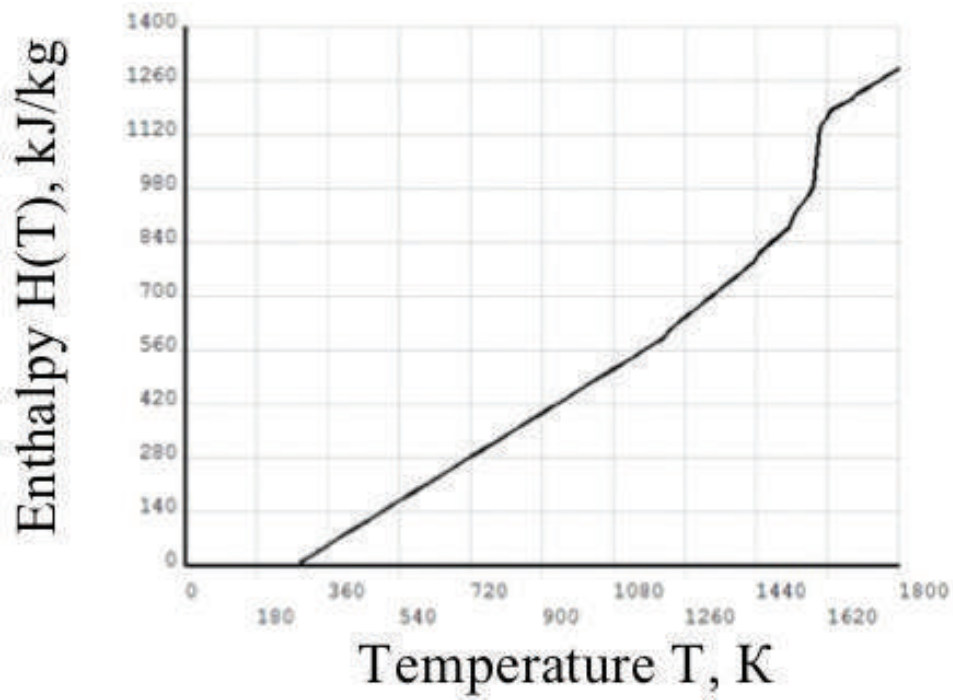


Figure 12. Dependence of the enthalpy  $H(T)$ ,  $\text{kJ/kg}$ , from the temperature  $T$ ,  $\text{K}$ , for the alloy Inconel 718.

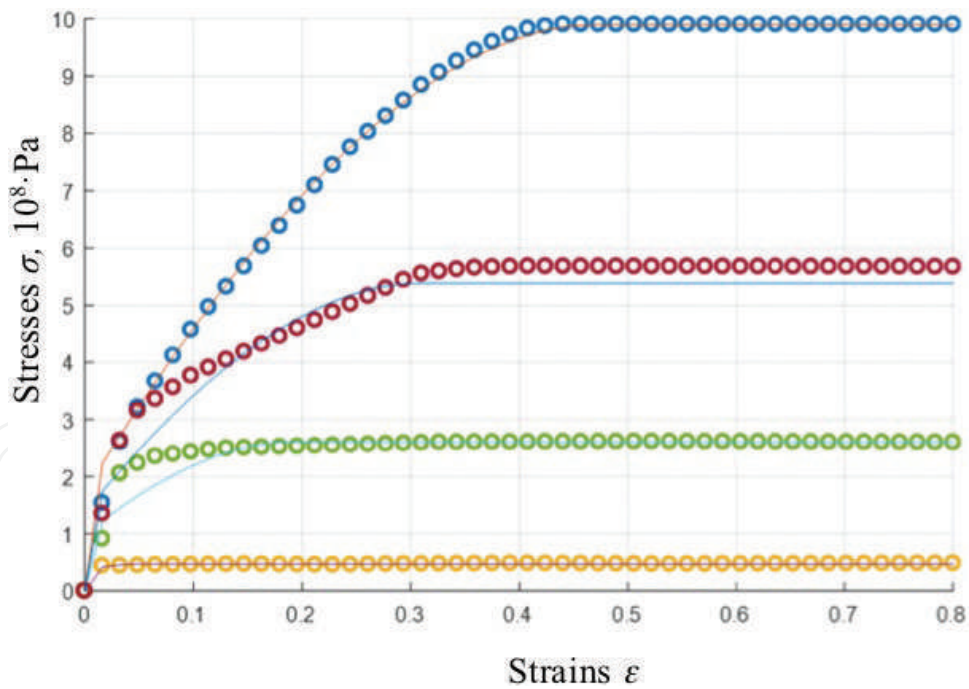


Figure 13. Comparison of experimental (dots) and computational values of voltage in unconfined stretch tests at the temperatures of 720, 850, 900, 1150°C (top-down).

Figure 13 shows that relative error of the calculation does not exceed 10%. The material was considered as isotropic. The Young's modulus of elasticity and the Poisson ratio were equal to 153 GPa and 0.32 respectively and not dependent on temperature [80]. The average value of

CLTE at the temperature range up to the solidus temperature  $\alpha$  is  $6.5 \times 10^{-6} \text{ K}^{-1}$ . The lineal shrinkage on the interval between solidus and liquidus temperatures is 0.3% and included in the temperature dependence  $\alpha(T)$ . Hardening and softening effects, accompanying the building up process, are included into the Anand model.

The main results of the calculations were given in [88]. Verification was performed using the experimental results obtained in the paper [86, 87]. **Figure 14** shows the layout of temperature sensors in the investigational studies mentioned above.

In this case sensors No. 2, 3, 5, 6 were placed on the upper surface of the base plate, and No. 1 and 4 were placed on its bottom surface. Initial direction of the torch movement is from right to left. **Figures 15–17** show graphs of temperature evolution at the given points.

The figures show that the qualitatively retrieved data comply with the experiment. The worst quantitative match is observed at points on the down plane of the base close to the heating area (points 1 and 4, **Figure 15**). In addition, the curves have oscillations and the temperature is below the ambient temperature at some points. All in all, the experimental graphs are below the computational graphs. The oscillations can be explained by proximity of the heating area and, consequently, heavy temperature gradients substantially altering the result at a fairly coarse mesh. Higher heating level in the experiment may be also caused by failure to take account of the torch heat radiation expanded far beyond the computational size of the spot.

Precision of the computational data is substantially higher at other measurement points (**Figures 16 and 17**). The maximum absolute disparity does not exceed  $25^\circ\text{C}$ .

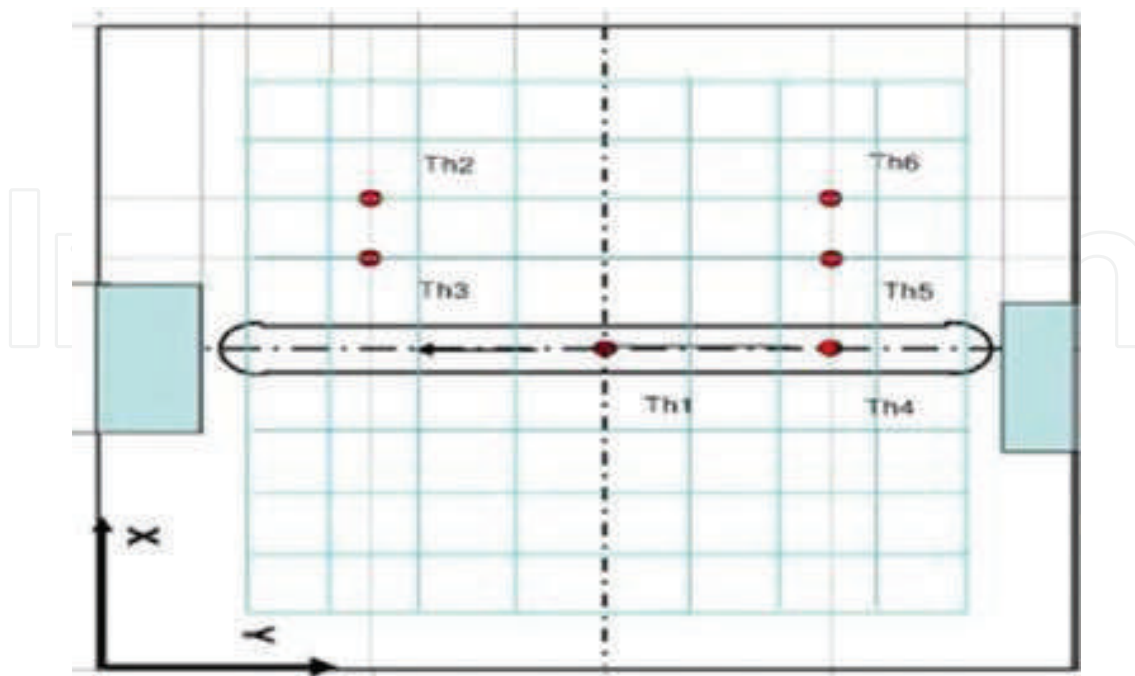


**Figure 14.** The layout of temperature sensors.

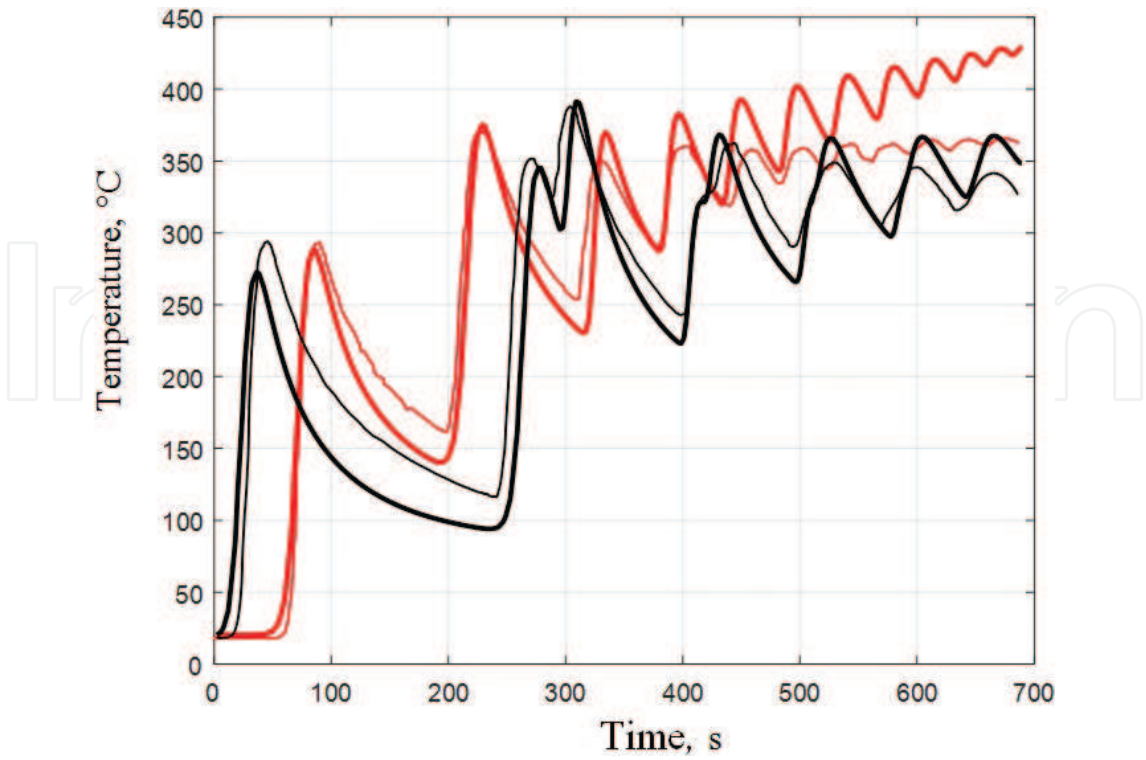


Figure 15. The temperature, °C in points 1 (red lined) and 4 (black lines). Thin curves show the experiment, thick curves show the calculation.

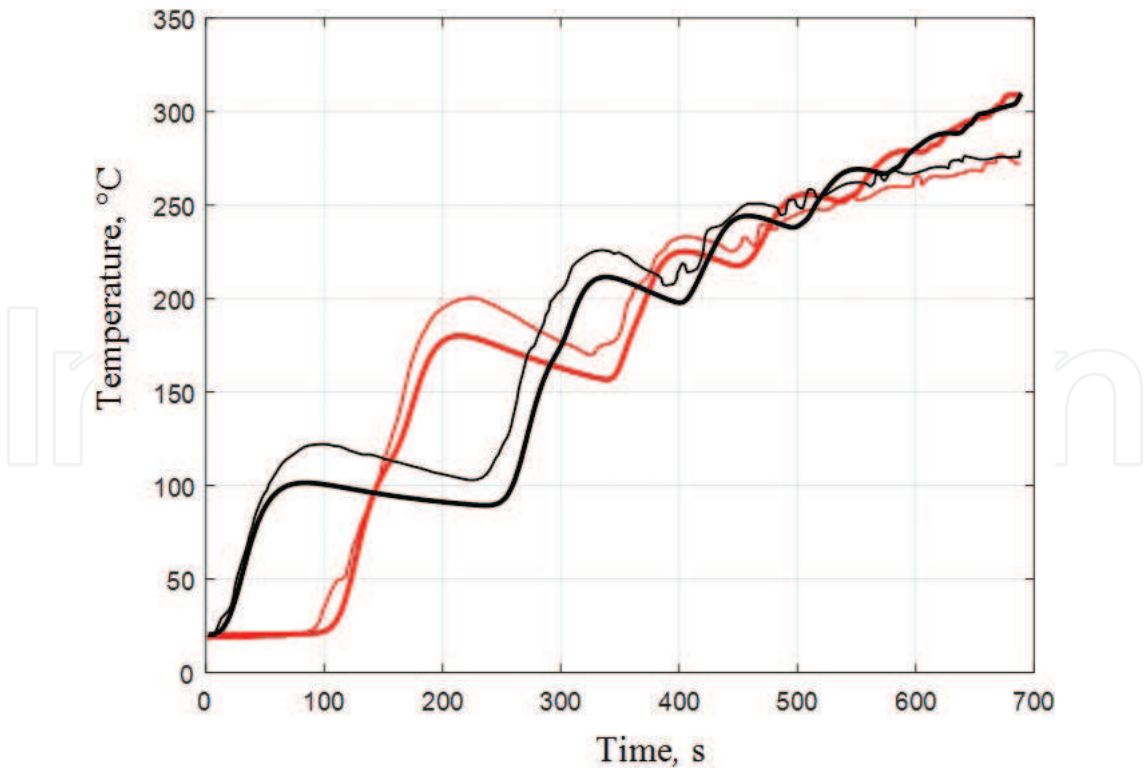
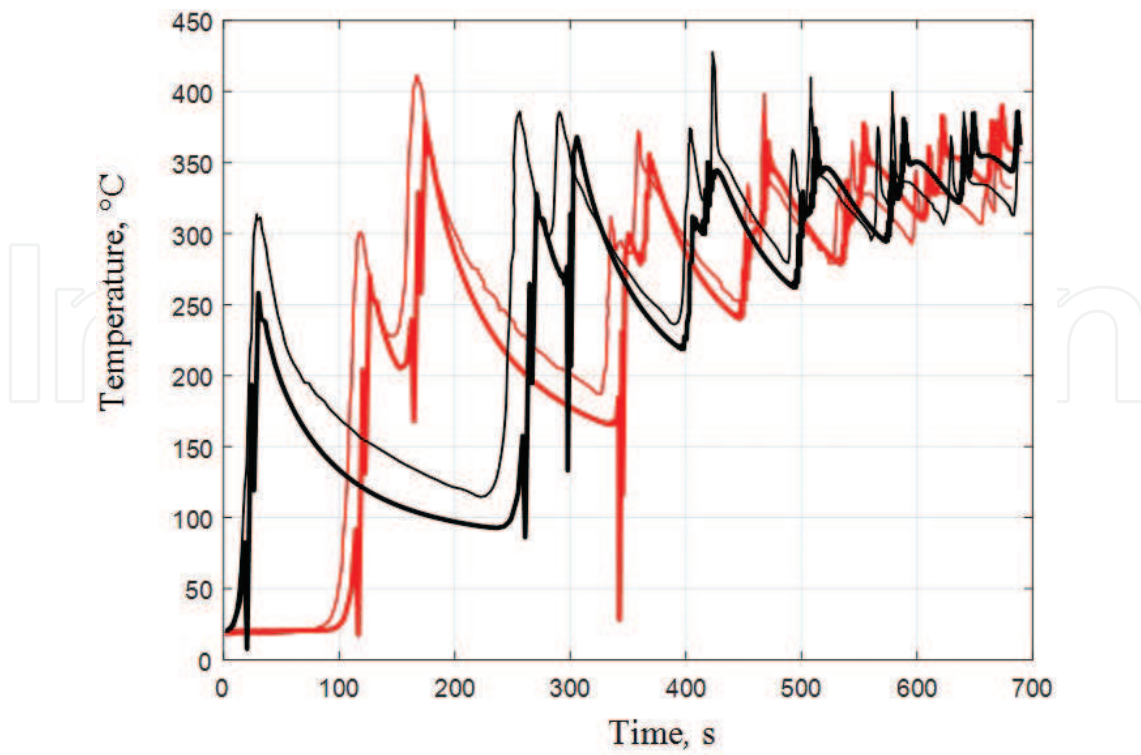
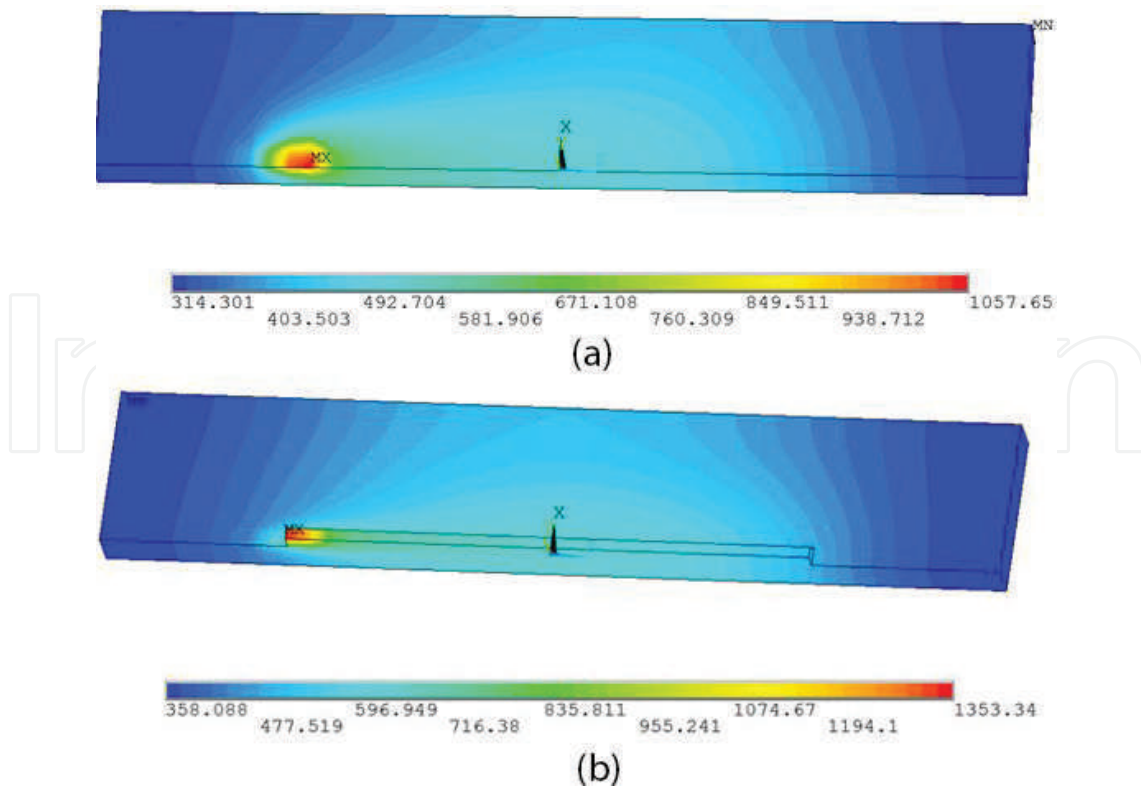


Figure 16. The temperature, °C in points 2 (red lined) and 6 (black lines). Thin curves—the experiment, thick curves—the calculation.



**Figure 17.** The temperature, °C in points 3 (red lined) and 5 (black lines). Thin curves—the experiment, thick curves—the calculation.



**Figure 18.** Temperature distribution, K (a)  $t = 291$  s, (b)  $t = 506$  s.

**Figure 18** shows by way of illustration the temperature fields at the moment of the end of preliminary heating of the base plate (**Figure 18a**) and of the end of the fourth layer (**Figure 18b**).

**Figure 19** shows the results of solution of the deformable body mechanics problem and residual displacement at central cross sections of the plate. The figure shows that the residual contraction of the structure can be estimated with acceptable accuracy. It was predicted that the plate will be bowl-shaped with the height of the ribs about 1 mm. The minimum computational accuracy is at the cross section where the relative disparity of the height runs up to 20%.

**Figure 20** represents the distribution pattern of residual characteristics in the structure.

**Figure 20a** shows that the longitudinal bend dominates. The transverse bend is almost 10 times lower. The maximum intensity of residual stresses is observed at the contact area of the deposited material and the base.

The stresses are calculated at every step of solution of the quasipermanent boundary deformable solid body problem (Eqs. (21)–(28)). **Figure 20b** represents distribution of residual stresses, i.e. the stresses observed in the structure at the end of the production process and complete cooldown to the ambient temperature.

The model of thermomechanical behavior of the sample, created by the additive fabrication method, is designed for evaluation of strain-stress state of the sample and its contraction as well as for definition of parameters of the production process ensuring low contraction and residual stress. The model can be combined with other mathematical and numerical models

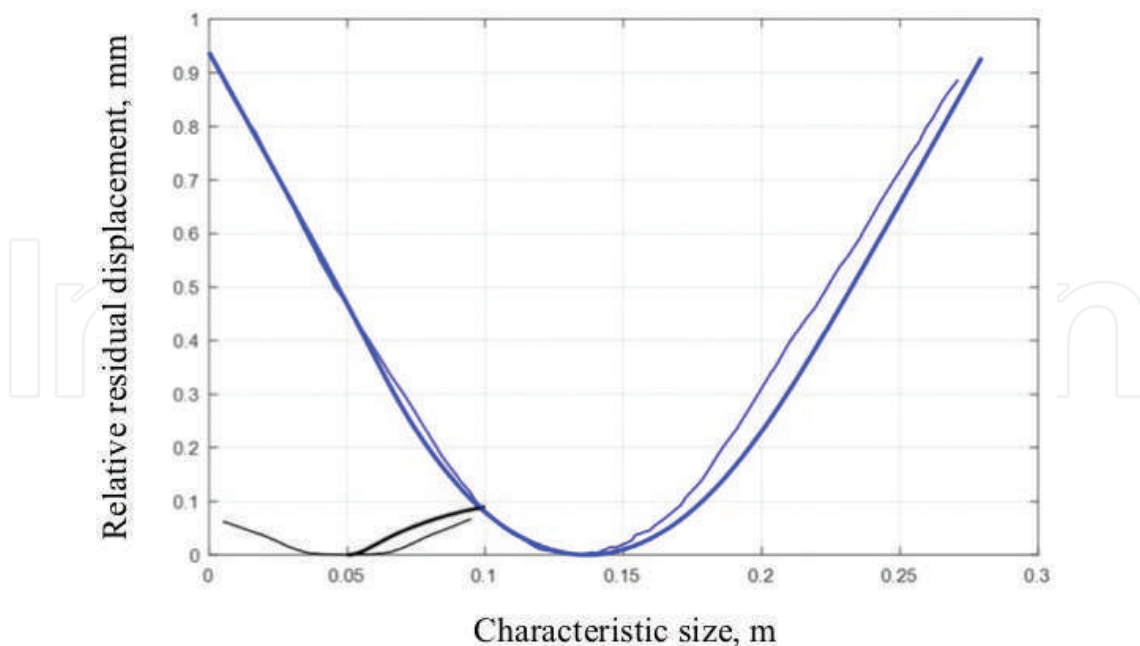


**Figure 19.** Relative residual displacement, mm, at longitudinal (blue lines) and cross (black lines) sections of the plate on its bottom surface. Thin curves show the experiment, thick curves show the calculation.

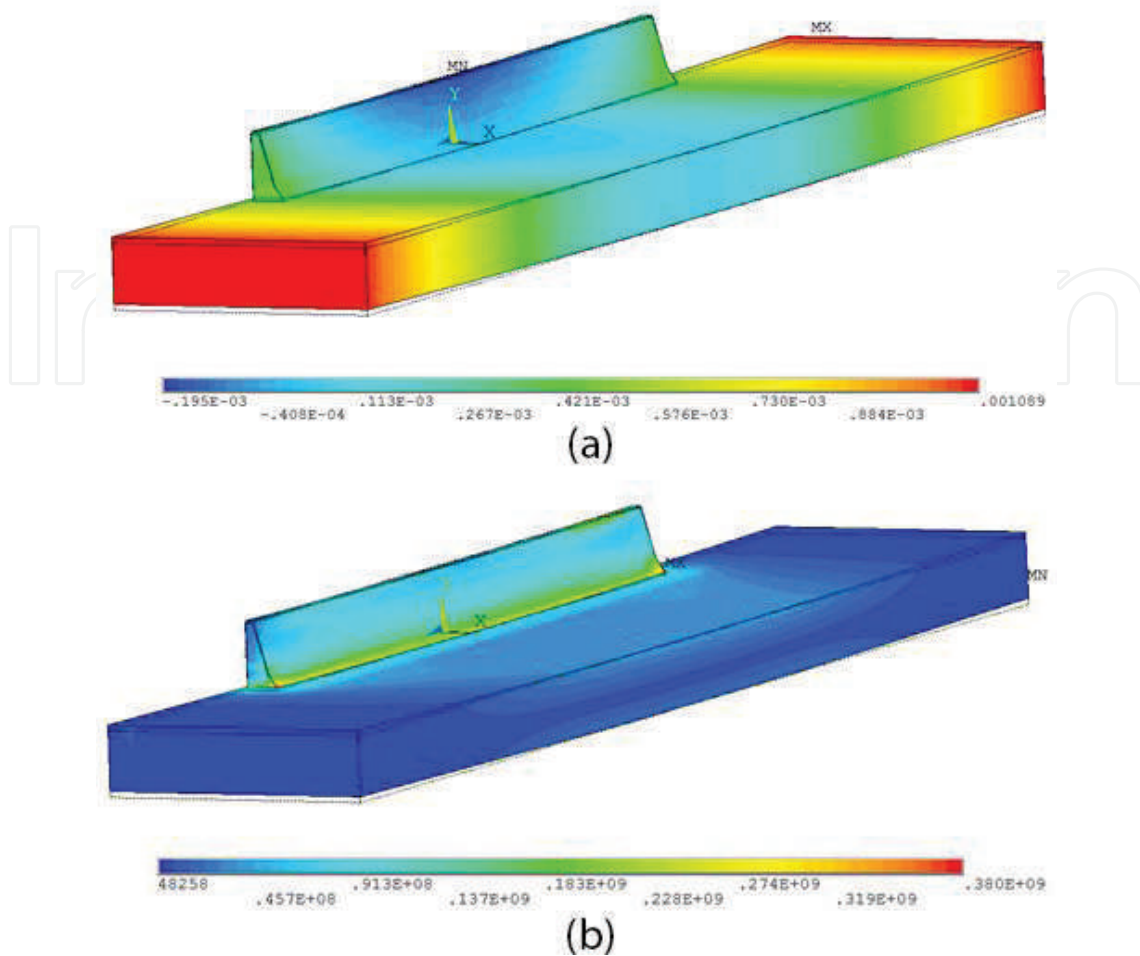


**Figure 20.** Vertical displacement in the structure after its cooldown and release, m (a), residual stress intensity, Pa (b).

including the temperature and conversion model specifying distribution of the variable temperature field inside the sample.

The model may be included into a computer-aided expert system to forecast the results of additive fabrication of large-sized components.

## 5. Conclusions

1. We defined the mathematical problem (model) of heat and mass transfer in the process of additive fabrication of products by fusion of wire material using plasma (electric) arc and concentrated energy sources with asymmetrical wire feed. The model describes transient nonequilibrium adjoint heat and mass transfer processes in molten metal with free surface, includes differential equation of viscous fluid movement (Navier-Stokes equations) with

convective terms in laminar current, takes into account the Marangoni effect on the surface of melt, and allows to calculate volume distribution of temperatures, melt flow speed, pressure, shape and dimensions of the molten pool, shape of the molten metal free surface, shape and dimensions of the deposited bead. We also defined potential uses of the models.

2. We suggested approximation of the wire feed process by mass inflow on the metal-gas edge. To describe movement of the molten-solid metal interface, one can use any of the two following methods: the Level-Set method or the Arbitrary Lagrangian-Eulerian method (ALE).
3. We described the heat source when using a plasma arc of various electrical polarity. In the process of deposition with reverse polarity, the plasma source is represented by a combination of the source of the heat, transferred by the plasma flow, with Gaussian distribution and a uniformly distributed source in the area of cathode spots impact. The energy relation between the sources is defined by experiment. We preselected the approximating formulas which describe influence of technological parameters of plasma arcs on distribution of heat flow density in the source.
4. We suggested the mathematical 3D-model of the additive product fabrication process by deposition of wire material.
5. We developed and implemented in the form of an APDL program in the ANSYS package the algorithm for estimation of unsteady temperature fields and strain-stress state of the structure in the process of its generation by arc 3D-deposition of wire materials.
6. The experimental information of other authors was used to identify the thermal-physical and thermomechanical properties of the material—the Inconel 718 nickel alloy.
7. Verification of the model showed required accuracy of the results.
8. The represented example of application of the model and its numerical implementation in the ANSYS package shows that the chosen approach is reasonable and allows to obtain acceptable numerical results properly describing real effects and processes in the objects created by the method of additive volume generation. More accurate verification procedure for the suggested mathematical model showing its accuracy and limits of applicability on the basis of experimental studies of residual stresses and thermoshrinkable deformations of model products manufacturing using the method of additive part fabrication by fusion of wire material with an electric arc and concentrated energy sources will be represented in future studies.

## Acknowledgements

The work was supported by the Ministry of Education and Science of the Russian Federation (RFMEFI58317X0062) and MOST (No. 2017YFE0100100) under the BRICS project.

## Author details

Dmitriy Trushnikov<sup>1\*</sup>, Oleg Smetannikov<sup>2</sup>, Anatoly Perminov<sup>3</sup>, Shengyong Pang<sup>4</sup>, Karuppasamy Poolan Karunakaran<sup>5</sup>, Petr Maksimov<sup>2</sup>, Mariia Bartolomey<sup>2</sup>, Aleksei Kovyazin<sup>2</sup>, Vladimir Belenkiy<sup>6</sup> and Yurii Schitsyn<sup>1</sup>

\*Address all correspondence to: [trdimitr@yandex.ru](mailto:trdimitr@yandex.ru)

1 Department of Welding Production, Metrology and Technology of Material, Mechanical Engineering Faculty, Perm National Research Polytechnic University, Perm, Russia

2 Department of Computational Mathematics and Mechanics, Faculty of Applied Mathematics and Mechanics, Perm National Research Polytechnic University, Perm, Russia

3 Department of General Physics, Faculty of Applied Mathematics and Mechanics, Perm National Research Polytechnic University, Perm, Russia

4 State Key Laboratory of Materials Processing and Die and Mould Technology, Huazhong University of Science and Technology, Wuhan, China

5 Department of Mechanical Engineering, Rapid Manufacturing Laboratory, Indian Institute of Technology Bombay, Mumbai, India

6 Mechanical Engineering Faculty, Perm National Research Polytechnic University, Perm, Russia

## References

- [1] Sciaky Inc. Electron Beam Additive Manufacturing (EBAM)—Advantages of Wire AM vs. Powder AM. URL: <http://additivemanufacturing.com/2015/10/14/electron-beam-additive-manufacturing-ebamadvantages-of-wire-am-vs-powder-am>
- [2] Sciaky Inc. Electron Beam Additive Manufacturing (EBAM). URL: <http://www.sciaky.com/images/pdfs/product-sheets/Sciaky-EBAM-Technology.pdf>
- [3] Jhavar S, Jain NK, Paul CP. Development of micro-plasma transferred arc (p-PTA) wire deposition process for additive layer manufacturing applications. *Journal of Materials Processing Technology*. 2014;**214**(5):1102-1110
- [4] Louvis E et al. Selective laser melting of aluminium components. *Journal of Materials Processing Technology*. Department of Engineering, The University of Liverpool, Liverpool L69 3GH, United Kingdom. 2011;**211**:275-284
- [5] Campanelli SL et al. Capabilities and Performances of the Selective Laser Melting Process. Polytechnic of Bari, Department of Management and Mechanical Engineering, Viale Japigia, 182 Italy [electronic source]. URL: <http://cdn.intechopen.com/pdfs/12285/InTech->

Capabilities\_and\_performances\_of\_the\_selective\_laser\_melting\_process.pdf Three-dimensional Printing and Additive Manufacturing of High-performance Metals and Alloys

- [6] Yu A. Bezobrazov, Zlenko MA, Zotov OG, et al. Analysis of the structure of samples obtained by DMLS and SLM methods of rapid prototyping. In: Innovative Technologies in Metallurgy and Machine Building: Materials of the 6th International Youth Scientific and Practical Conference in Innovative Technologies in Metallurgy and Machine Building. Ural Scientific and Pedagogical School n.a. Professor A.F. Golovin [the city of Ekaterinburg, October 29–November 1, 2012]; Ekaterinburg: Ural University Publishing House; 2012. pp. 154-157
- [7] Qiu C, Panwisawas C, Ward M, Basoalto HC, Brooks JW, Attallah MM. On the role of melt flow into the surface structure and porosity development during selective laser melting. *Acta Materialia*. September 1, 2015; **96**:72-79. DOI: 10.1016/j.actamat.2015.06.004. ISSN 1359-6454 (<http://www.sciencedirect.com/science/article/pii/S1359645415003870>)
- [8] Kapil S, Legesse F, Kulkarni PM, Joshi P, Desai A, Karunakaran KP. Hybrid layered manufacturing using tungsten inert gas cladding. *Progress in Additive Manufacturing*. 2016; **1**(1):79-91
- [9] Zhang Y, Bernard A, Harik R, Karunakaran KP. Build orientation optimization for multipart production in additive manufacturing. *Journal of Intelligent Manufacturing*. 2017; **28**(6): 1393-1407
- [10] Amine T, Newkirk JW, Liou F. Investigation of effect of process parameters on multilayer builds by direct metal deposition. *Applied Thermal Engineering*. 2014; **73**(1):500-511
- [11] Hu YP, Chen CW, Mukherjee K. Measurement of temperature distributions during laser cladding process. *Journal of Laser Applications*. 2000; **12**(3):126-130
- [12] Shishkovsky IV, Scherbakov VI, Morozov YG, Kuznetsov MV, Parkin IP. Surface laser sintering of exothermic powder compositions. *Journal of Thermal Analysis and Calorimetry*. 2008; **91**(2):427-436
- [13] Benda J. Temperature controlled selective laser sintering. In: *Proceedings of the Solid Freeform Fabrication Symposium*; 1994. pp. 277-284
- [14] Doubenskaia M, Pavlov M, Chivel Y. Optical system for on-line monitoring and temperature control in selective laser melting technology. *Key Engineering Materials*. 2010; **437**: 458-461
- [15] Hu DM, Kovacevic R. Sensing, modeling and control for laser-based additive manufacturing. *International Journal of Machine Tools & Manufacture*. 2003; **43**(1):51-60
- [16] Jian X, Jinghua S, Yiqing G. Novel measurement method for selective laser sintering transient temperature field. In: *3rd International Symposium on Advanced Optical Manufacturing and Testing Technologies: Optical Test and Measurement Technology and Equipment*; 2007. pp. 67234N-67234N

- [17] Price S, Cooper K, Chou K. Evaluations of temperature measurements by near-infrared thermography in powder-based electron-beam additive manufacturing. In: Proceedings of the Solid Freeform Fabrication Symposium. Austin (TX): University of Texas; 2012. pp. 761-773
- [18] Mughal MP, Fawad H, Mufti RA, Siddiqui M. Deformation modelling in layered manufacturing of metallic parts using gas metal arc welding: Effect of process parameters. *Modeling and Simulation in Materials Science and Engineering*. 2005;**13**(7):1187-1204
- [19] Beuth VA, JL GM. Process maps for predicting residual stress and melt pool size in the laser-based fabrication of thin-walled structures. *Journal of Manufacturing Science and Engineering*. 2007;**129**(1):101-109
- [20] Manvatkar V, De A, DebRoy T. Heat transfer and material flow during laser assisted multi-layer additive manufacturing. *Journal of Applied Physics*. 2014;**116**(12):1-8. Article No. 124905
- [21] Svensson LE, Grefott B, Bhadeshia HKDH. An analysis of cooling curves from the fusion zone of steel weld deposits. *Scandinavian Journal of Metallurgy*. 1986;**15**(2):97-103
- [22] Markl M, Korner C. Multiscale modeling of powder bed-based additive manufacturing. *Annual Review of Materials Research*. 2016;**46**:93-123
- [23] Manvatkar V, De A, DebRoy T. Spatial variation of melt pool geometry, peak temperature and solidification parameters during laser assisted additive manufacturing process. *Materials Science and Technology*. 2015;**31**(8):924-930
- [24] Raghavan A, Wei HL, Palmer TA, DebRoy T. Heat transfer and fluid flow in additive manufacturing. *Journal of Laser Applications*. 2013;**25**(5):1-8. Article No. 052006
- [25] Patankar S. *Numerical Heat Transfer and Fluid Flow*. Hemisphere, New York: CRC Press; 1980
- [26] King W, Anderson A, Ferencz R, Hodge N, Kamath C, Khairallah S. Overview of modeling and simulation of metal powder bed fusion process at Lawrence Livermore National Laboratory. *Materials Science and Technology*. 2015;**31**(8):957-968
- [27] Li C, Wang Y, Zhan H, Han T, Han B, Zhao W. Three-dimensional finite element analysis of temperatures and stresses in wide-band laser surface melting processing. *Materials & Design*. 2010;**31**(7):3366-3373. DOI: 10.1016/j.matdes.2010.01.054
- [28] Ma L, Bin H. Temperature and stress analysis and simulation in fractal scanning-based laser sintering. *International Journal of Advanced Manufacturing Technology*. 2007;**34**(9): 898-903
- [29] Roberts IA et al. Experimental and numerical analysis of residual stresses in additive layer manufacturing by laser melting of metal powders [Электронный документ]. *Key Engineering Materials*. 2011;**450**:461-465. DOI: 10.4028/www.scientific.net/KEM.450.461 (<http://32www.scientific.net/KEM.450.461>). Проверено 14.10.2017

- [30] Parry L, Ashcroft I, Bracket D, Wildman RD. Investigation of residual stresses in selective laser melting. *Key Engineering Materials*. 2015;**627**:129-132
- [31] Wu A, Brown D, Kumar M, Gallegos G, King W. An experimental investigation into additive manufacturing-induced residual stresses in 316L stainless steel. *Metallurgical and Materials Transactions*. 2014;**45A**:1-11
- [32] Baufeld B, Van der Biest O, Gault R. Additive manufacturing of Ti–6Al–4V components by shaped metal deposition: Microstructure and mechanical properties. *Materials & Design*. 2010;**31**:106-111
- [33] Riedlbauer D, Mergheim J, McBride A, Steinmann P. Macroscopic modelling of the selective beam melting process. *Proceedings in Applied Mathematics and Mechanics*. 2012;**12**(1): 381-382
- [34] Labudovic M, Hu D, Kovacevic R. A three dimensional model for direct laser metal powder deposition and rapid prototyping. *Journal of Materials Science*. 2003;**38**(1):35-49
- [35] Hodge NE, Ferencz RM, Solberg JM. Implementation of a thermomechanical model for the simulation of selective laser melting. *Computational Mechanics*. 2014;**54**(1):33-51
- [36] Denlinger ER, Michaleris P. Effect of stress relaxation on distortion in additive manufacturing process modeling. *Additive Manufacturing*. 2016;**12**:51-59
- [37] Korner C. Additive manufacturing of metallic components by selective electron beam melting—A review. *International Materials Review*. 2016;**61**(5):361-377
- [38] Prabhakar P, Sames W, Dehoff R, Babu S. Computational modeling of residual stress formation during the electron beam melting process for Inconel 718. *Additive Manufacturing*. 2015;**7**:83-91
- [39] Neulybin SD, Permyakov LD, Trushnikov DN, Shchitsyn YD, Belenkiy VY. Development of a dynamic model of thermal processes for plasma surfacing at direct and reverse polarity. *International Journal of Applied Engineering Research*. 2017;**12**(22):11847-11854
- [40] Asai S, Muchi I. Theoretical analysis and model experiments on the formation mechanism of channel-type segregation. *Transactions of the Iron and Steel Institute of Japan*. 1978;**18**(2):90-98
- [41] Kharitonov IA, Martynov VN, Shcherbakov AV, Dragunov VK, Gaponova DA. The Second International Conference on Electron Beam Welding and Related Technologies; November 14–17, 2017; National Research University Moscow Power Engineering Institute: Collection of Materials and Reports. pp. 257-265
- [42] Bennon WD, Incropera FP. A continuum model for momentum, heat and species transport in binary solid-liquid phase change systems. I. Model formulation. *International Journal of Heat and Mass Transfer*. 1987;**30**:2161-2169
- [43] Qi H, Mazumder J, Ki H. Numerical simulation of heat transfer and fluid flow in coaxial laser cladding process for direct metal deposition. *Journal of Applied Physics*. 2006;**100**(2): 024903

- [44] Gan Z, Yu G, He X, Li S. Surface-active element transport and its effect on liquid metal flow in laser-assisted additive manufacturing. *International Communications in Heat and Mass Transfer*. 2017;**86**:206-214
- [45] He X, Mazumder J. Transport phenomena during direct metal deposition. *Journal of Applied Physics*. 2007;**101**:053-113
- [46] Shchitsyn VY, Yazovskikh VM. Influence of polarity on heat input into the nozzle of a plasma torch. *Welding Production*. 2002;**1**:17-19
- [47] Sosnin NA, Ermakov SA, Topolyansky PA. *Plasma Technologies. Manual for Engineers*. SPb: Publishing House of Polytechnic University; 2008. p. 406
- [48] Vainerman AE, Zakharov VF, Prilukov VN, Syutev AN. Surfacing with a compressed arc of a reverse polarity of chromium-nickel steel on structural steels. In: *Plasma Methods of Metal Processing*. Leningrad: Leningrad Publishing House of Scientific and Technical Propaganda; 1977. pp. 27-34
- [49] Vainerman AE, Krasulin YL, Shorshorov MK. Plasma surfacing of copper and bronze on steel with a plasma jet. In: *Automatic Welding*, Leningrad [without publisher]; 1966. p. 35
- [50] Neubybin SD. Influence of current polarity of the properties of layered materials obtained by multilayer plasma surfacing [Text]: PhD Thesis in Technical Sciences of February 5, 2010—Welding, Related Processes and Technologies; Perm National Research Polytechnic University—Perm, 2017. p.135
- [51] Harvey PD, editor. *Engineering Properties of Steels*. Metals Park, OH: American Society for Metals; 1982
- [52] Peckner D, Bernstein IM. *Handbook of Stainless Steels*. New York, NY: McGraw-Hill Book Company; 1977
- [53] Boyer HE, Gall TL, editors. *Metals Handbook*. Materials Park, OH: American Society for Metals; 1985
- [54] ASM International Handbook Committee. *Metals Handbook*. 10th ed. Vol. 1. Materials Park, OH: ASM International; 1990
- [55] Shchitsyn YD, Kosolapov OA, Strukov NN. Energy distribution of a compressed arc during the operation of a plasma torch of a reverse polarity. *Welding and Diagnostics*. 2010;**3**:13-16
- [56] King W, Anderson A, Ferencz R, Hodge N, Kamath C, Khairallah S. Overview of modeling and simulation of metal powder bed fusion process at Lawrence Livermore National Laboratory. *Materials Science and Technology*. 2015;**31**(8):957-968
- [57] Li C, Wang Y, Zhan H, Han T, Han B, Zhao W. Three-dimensional finite element analysis of temperatures and stresses in wide-band laser surface melting processing. *Materials & Design*. 2010;**31**(7):3366-3373. DOI: 10.1016/j.matdes.2010.01.054
- [58] Roberts IA et al. Experimental and numerical analysis of residual stresses in additive layer manufacturing by laser melting of metal powders [electronic document]. *Key Engineering*

Materials. 2011;**450**:461-465. DOI: 10.4028/www.scientific.net/KEM.450.461 (<http://www.scientific.net/KEM.450.461>). Reviewed on October 14, 2017

- [59] Martukanitz R, Michaleris P, Palmer T, DebRoy T, Liu Z-K, Otis R, et al. Toward an integrated computational system for describing the additive manufacturing process for metallic materials. *Additive Manufacturing*. 2014;**1**:52-63
- [60] Michaleris P. Modeling metal deposition in heat transfer analyses of additive manufacturing processes. *Finite Elements in Analysis and Design*. 2014;**86**:51-60
- [61] Papadakis L, Loizou A, Risse J, Schrage J. Numerical computation of component shape distortion manufactured by selective laser melting. *Procedia CIRP*. 2014;**18**:90-95. DOI:03 10.1016/j.procir.2014.06.1 13
- [62] Shishkovsky IV, Volynsky I. Experimental and numerical modelling of function-graded porous filter elements, synthesized by the SLS method. In: *High Value Manufacturing: Advanced Research in Virtual and Rapid Prototyping: Proceedings of the 6th International Conference on Advanced Research in Virtual and Rapid Prototyping, Leiria, Portugal; October 1–5, 2013*. p. 55
- [63] Alimardani M, Toyserkani E, Huissoon JP. A 3D dynamic numerical approach for temperature and thermal stress distributions in multilayer laser solid freeform fabrication process. *Optics and Lasers in Engineering*. 2007;**45**(12):1115-1130
- [64] Beuth J, Klingbeil N. The role of process variables in laser-based direct metal solid freeform fabrication. *JOM*. 2001;**53**(9):36-39
- [65] Wang L, Felicelli SD, Pratt P. Residual stresses in LENS-deposited AISI 410 stainless steel plates. *Materials Science and Engineering A*. 2008;**496**(1-2):234-241
- [66] Ghosh S, Choi J. Three-dimensional transient finite element analysis for residual stresses in the laser aided direct metal/material deposition process. *Journal of Laser Applications*. 2005;**17**(3):144-158
- [67] Ghosh S, Choi J. Modeling and experimental verification of transient/residual stresses and microstructure formation in multi-layer laser aided DMD process. *Journal of Heat Transfer*. 2006;**128**(7):662-679
- [68] Farahmand P, Kovacevic R. An experimental-numerical investigation of heat distribution and stress field in single- and multi-track laser cladding by a high-power direct diode laser. *Optics and Laser Technology*. 2014;**63**:154-168
- [69] Ding J, Colegrove P, Mehnen J, Ganguly S, Almeida PMS, Wang F, et al. Thermomechanical analysis of wire and arc additive layer manufacturing process on large multi-layer parts. *Computational Materials Science*. 2011;**50**(12):3315-3322
- [70] Zhao XM, Chen J, Lin X, Huang WD. Study on microstructure and mechanical properties of laser rapid forming Inconel 718. *Materials Science and Engineering A*. 2008;**478**(1-2): 119-124

- [71] Mukherjee T, Zuback JS, De A, DebRoy T. Printability of alloys for additive manufacturing. *Scientific Reports*. 2016;**6**:1-8. Article No. 9717
- [72] Martina F, Mehnen J, Williams SW, Colegrove P, Wang F. Investigation of the benefits of plasma deposition for the additive layer manufacture of Ti-6Al-4V. *Journal of Materials Processing Technology*. 2012;**212**(6):1377-1386
- [73] Chiumenti M, Cervera M, Salmi A, de Saracibar CA, Dialami N, Matsui K. Finite element modeling of multi-pass welding and shaped metal deposition processes. *Computer Methods in Applied Mechanics and Engineering*. 2010;**199**(37-40):2343-2359
- [74] Denlinger ER, Irwin J, Michaleris P. Thermomechanical modeling of additive manufacturing large parts. *Journal of Manufacturing Science and Engineering*. 2014;**136**(6):061007
- [75] Mukherjee T, Manvatkar V, De A, DebRoy T. Mitigation of thermal distortion during additive manufacturing. *Scripta Materialia*. 2017;**127**:79-83
- [76] Goldak JA, Akhlaghi M. *Computational Welding Mechanics*. 1st ed. US: Springer; 2006
- [77] Ding J, Colegrove P, Mehnen J, Williams S, Wang F, Almeida PS. A computationally efficient finite element model of wire and arc additive manufacture. *International Journal of Advanced Manufacturing Technology*. 2014;**70**(1-4):227-236
- [78] Li C, Fu C, Guo Y, Fang F. A multiscale modeling approach for fast prediction of part distortion in selective laser melting. *Journal of Materials Processing Technology*. 2016;**229**: 703-712
- [79] Yuan MG, Ueda Y. Prediction of residual stresses in welded T- and I-joints using inherent strains. *Journal of Engineering Materials and Technology*. 1996;**118**(2):229-234
- [80] INCONEL<sup>®</sup> alloy 718 properties. Special Metals. Url: <http://www.specialmetals.com/15/assets/smc/documents/alloys/inconel/inconel-alloy-718.pdf>
- [81] Mohanty S, Hattel JH. Numerical model based reliability estimation of selective laser melting process. *Physics Procedia*. 2014;**56**:379-389. DOI: 10.1016/j.phpro.2014.08.135
- [82] Ilin A, Logvinov R, Kulikov A, Prihodovsky A, Xu H, Ploshikhin V, Gunther B, Bechmann F. Computer aided optimisation of the thermal management during laser beam melting process. *Physics Procedia*. 2014;**56**:390-399. DOI: 10.1016/j.phpro.2014.08.142
- [83] Kaplan AFH, Norman P, Eriksson I. Analysis of the keyhole and weld pool dynamics by imaging evaluation and photodiode monitoring. In: *Proceedings of LAMP2009—the 5th International Congress on Laser Advanced Materials Processing*; 2009. pp. 1-6
- [84] Askaryan GA, Morozov EM. Pressure in the evaporation of a substance in ray-radiation. *Journal of Experimental and Theoretical Physics*. 1962;**43**(6):2319-2320
- [85] Agelet de Saracibar C, Lundbäck A, Chiumenti M, Cervera M. Shaped metal deposition processes. In: *Encyclopedia of Thermal Stresses*. Dordrecht: Springer; 2014. pp. 4346-4355. DOI: 10.1007/978-94-007-2739-7\_808

- [86] Overfelt RA, Sahai V, Ko YK, Berry JT. Porosity in cast equiaxed alloy 718 Superalloys 718, 625, 706 and Various Derivatives. In: Proceedings of the International Symposium on Superalloys 718, 625, 706 and Various Derivatives, Pittsburg, Pennsylvania; 1994. pp. 189-200
- [87] Nowotnik A, Pędrak P, Sieniawski J, Góral M. Mechanical properties of hot deformed Inconel 718 and X750. *Journal of Achievements in Materials and Manufacturing Engineering*. 2012;**50**(2):74-80
- [88] Smetannikov OY, Trushnikov DN, Maksimov PV, Bartolomey ML, Kovyazin AV. Modeling of the thermomechanical behavior of the product during process of 3D deposition of wire materials in ANSYS. *PNRPU Mechanics Bulletin*. 2017;**4**:154-172. DOI: 10.15593/04 perm.mech/2017.4.11

# We are IntechOpen, the world's leading publisher of Open Access books Built by scientists, for scientists

6,300

Open access books available

171,000

International authors and editors

190M

Downloads

Our authors are among the

154

Countries delivered to

TOP 1%

most cited scientists

12.2%

Contributors from top 500 universities



WEB OF SCIENCE™

Selection of our books indexed in the Book Citation Index  
in Web of Science™ Core Collection (BKCI)

Interested in publishing with us?  
Contact [book.department@intechopen.com](mailto:book.department@intechopen.com)

Numbers displayed above are based on latest data collected.  
For more information visit [www.intechopen.com](http://www.intechopen.com)



---

# Theory and Technology of Direct Laser Deposition

---

Gleb Turichin and Olga Klimova-Korsmik

Additional information is available at the end of the chapter

<http://dx.doi.org/10.5772/intechopen.76860>

---

## Abstract

Presently the additive technologies in manufacturing are widely developed in all industrialized countries. Replacing the traditional technology of casting and machining with additive technologies, one can significantly reduce material consumption and labor costs. They also allow obtaining products with desired properties. The most promising for manufacturing large-sized products is the additive technology of high-speed direct laser deposition. Using this technology allows to create complex parts and construction to one technological operation without using addition equipment and tools. This technology allows decreasing of consumption of raw materials and decrease amount of waste. Equipment for realization of DLD technology is universal and based on module design principle. DLD is based on layer-by-layer deposition and melting of powder by laser beam from using a sliced 3D computer-aided design (CAD) file. The materials used are powders based on Fe, Ni, and Ti. This chapter presents the results of machine design and research HS DLD technology from various materials.

**Keywords:** high-speed direct laser deposition, additive manufacturing, stability of process, equipment, structure, properties

---

## 1. Introduction

New manufacturing technologies are incorporated into most areas of engineering: aircraft industry, shipbuilding, medicine, engine construction, etc. Existing requirements for its demand are more energy efficient and have environmental compatibility; additive technologies meet both criteria. The intensive development of additive technologies in recent years makes it possible to improve the methods of manufacturing and processing products [1–5]. They allow saving expensive raw materials in comparison with classical production methods, during which up to 90% of the material can be removed. The issue of cost reduction is

especially relevant in knowledge-based industries (gas turbine engine construction, aviation, space exploration, etc.). Selective laser melting (SLM) technology has already been implemented in production in many countries of the world [6, 7]. However, SLM technology is limited by its inability to manufacture large-sized products and low productivity.

The main trend in the development of additive technology is to increase productivity while maintaining the required quality of the product. The most promising technology of product manufacturing is direct laser deposition analogue direct metal deposition (DMD), when the product is formed from a powder, which is supplied by compressed gas-powder jet directly into the laser action zone [8–11]. The jet can be as coaxial and as non-coaxial to focused laser beam, which provides heating and partial melting of the powder and heating the substrate. This technology allows to include a mixture of powders into the gas-powder jet and to change the composition of powders during the process.

The developed technology and equipment have several advantages in comparison with existing analogues. There is a high productivity of DLD process for the manufacture of real parts and products: up to 2.5 kg/h for nickel and iron alloys, up to 1.2 kg/h for titanium alloys. For similar equipment, the productivity is 2–3 times less [12–14]. There are experimental stands with the same high productivity (up to 2 kg/h), preferably [15]. The main feature of the developed equipment is a modular assembly type, which allows to modernize the installation at the customer's request. This is the first Russian technology and equipment for the implementation of additive production.

Complex studies were carried out to understand the relationship between the parameters of the process and the optimization of the technology for obtaining products with specified characteristics. As a result of the research done, the theory and technology of high-speed direct laser deposition are developed. Also a number of machines with various sizes are made for the implementation of this technology. Investigations for powder materials based on iron, nickel, and titanium demonstrated the possibility of obtaining high-quality parts and products. Also, the possibility of working with cermet materials is shown. The research results showed that developed technology of direct laser deposition can replace the currently used technologies, providing multiple increase productivity and material savings, in spite of its technological complexity.

## **2. Theory of high-speed direct laser deposition**

The processes that occur during high-speed laser deposition depend on a large number of distributed parameters which effect on the result [8]. An important aspect of the study is the stability of the direct laser deposition process. Previously, the authors studied the root peak formation in welds during the process of laser welding using highly concentrated energy fluxes. According to the present knowledge about the physical nature of these processes, the

reason for instabilities is self-oscillations of the weld pool [12–19]. Different experimental data confirm this idea [16, 19].

The stability of surface formation in the process of direct laser deposition is determined by the complex of physical processes occurring on the surface of the molten pool, which moves with high speed along the deposited product at a constant flow of matter to its surface. Hydrodynamic stability of melt flow in semiliquid bath, formed by substrate melting under laser beam heating and powder income, depends on driving force, which leads to melt motion. The main driving force for melt motion relative solid substrate in DLD process is Marangoni effect. Therefore velocity of liquid relative solid phase is determined by the rate of the thermocapillary flow [20]. To make the analysis more clear, it is convenient to confine to analyze practically interesting case, when the molten pool length “L” is much greater than its width “b” and depth “H,” which depend on parameters of deposition mode. Then analysis of the equation of continuity of the melt allows us to conclude that the “longitudinal” velocity component  $v_x$  directed along the axis of the laser beam motion relative to the target is much larger than transverse components  $v_y$  and  $v_z$  so we the boundary layer like flow. So that equation of the motion can be written in our case as

$$\frac{\partial v_x}{\partial t} + v_x \frac{\partial v_x}{\partial x} = -\frac{1}{\rho} \frac{\partial \rho}{\partial x} + v \frac{\partial^2 v_x}{\partial z^2} \quad (1)$$

At the “bottom” of the molten pool, which coincides with the previous layer surface, the “sticking” condition is fulfilled  $v_x|_{z=0} = 0$ ; on the surface, the continuity condition of the tangential component of the stress tensor is  $\eta \frac{\partial v_x}{\partial z}|_{z=H} = \frac{\partial \sigma}{\partial x}$ , where  $\sigma$  is the coefficient of surface tension. Assuming that at the front of the melt pool the surface temperature close to the boiling one and the surface tension value close to “0,” taking a linear law for the temperature drop to the “tail” of the melt pool, one can write

$$\eta \frac{\partial v_x}{\partial z} \Big|_{z=H} = \frac{\sigma}{L} \quad (2)$$

It is possible to get after a number of transformations that with the consideration of Marangoni force, Eq. (1) can be written in the next shape:

$$\frac{\partial v_x}{\partial t} + v_x \frac{\partial v_x}{\partial x} = -\frac{1}{\rho} \frac{\partial \rho}{\partial x} - 3v \frac{v_x}{H^2} + \frac{3\sigma}{2\rho LH} \quad (3)$$

One can use the mass conservation condition to connect the melt velocity  $v_x$  with position of the melt pool surface. Let  $\zeta$  be the height of the perturbation on surface. In our case, the mass flux coming to the melt surface with the gas-powder jet must be taken into account. One can denote the incident mass flux density on melt surface as  $j(x, \zeta)$ . Suppose  $\zeta \ll H$ , it is possible to write the continuity condition of the mass flux as

$$\frac{\partial v_x}{\partial x} \approx -\frac{1}{H} \frac{\partial \zeta}{\partial t} + \frac{j(x, 0)}{H\rho} + \frac{1}{H\rho} \frac{\partial j(x)}{\partial x} \zeta. \quad (4)$$

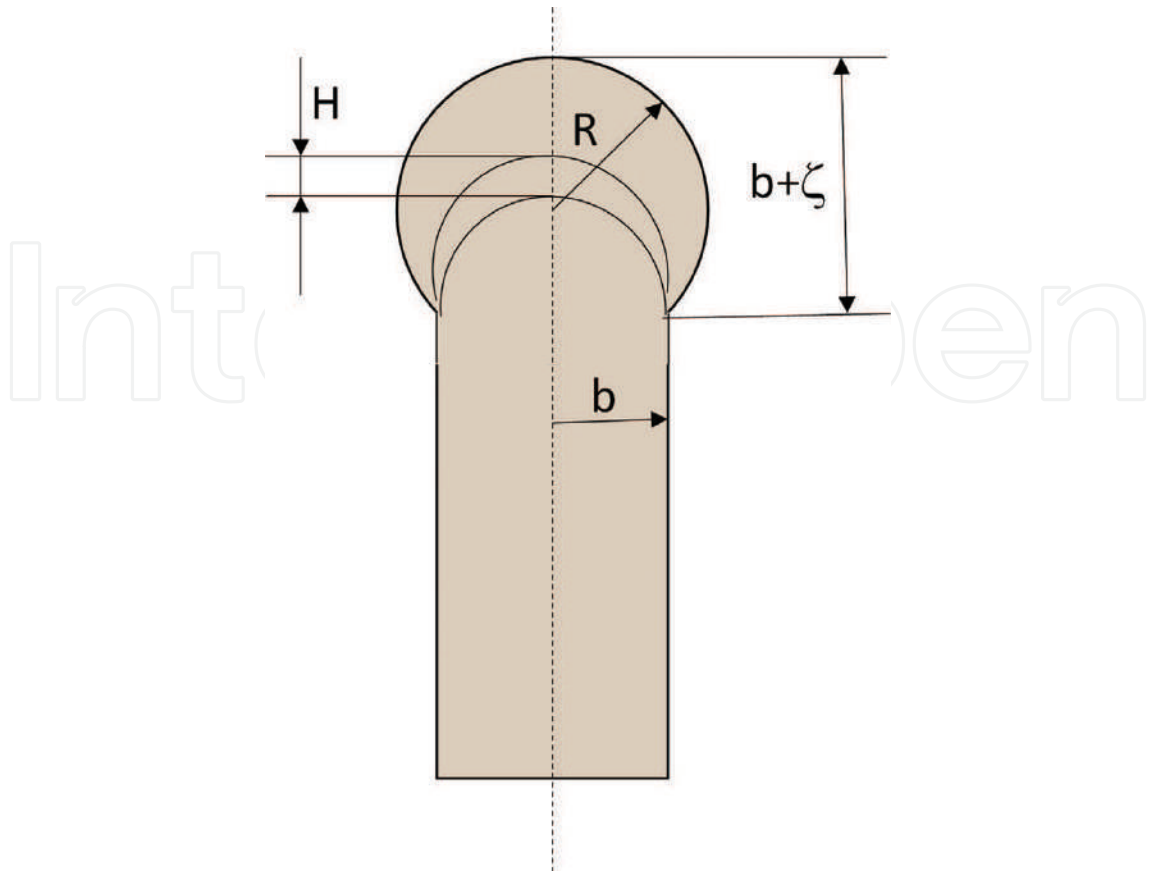


**Figure 1.** Geometry of the melt pool surface motion.

One can determine the Laplace pressure in the liquid “p” and the additional pressure, which is related to the perturbation of the melt pool surface  $\zeta$ , taking into account that  $p = \sigma/R$ , where R is the radius of surface curvature (**Figure 1**).

The one-dimensional model of thermocapillary flow does not allow introducing the effects of the influence of grown wall thickness on change in the shape of its surface. For that, we need to introduce a “transverse” dimension. Analysis of term scales in the continuity equation show that melt velocity in “transverse” direction is negligible but pressure changes can be significant. Therefore, when  $\zeta \ll H$ , one can get  $R \approx b + \frac{\zeta^2}{2b}$ , and for pressure it is possible to obtain  $p \approx \frac{\sigma}{b} = \frac{\sigma \zeta^2}{2b^3}$ .

Considering it, one can write Navier-Stokes equation in the two-dimensional case as

$$\frac{\partial v_x}{\partial t} + v_x \frac{\partial v_x}{\partial x} = -\frac{\sigma}{\rho} \frac{\partial^3 \zeta}{\partial x^3} - 3v \frac{v_x}{H^2} + \frac{3\sigma}{2\rho LH} + \frac{\sigma}{\rho b^3} \frac{\zeta \partial \zeta}{\partial x} \tag{5}$$

In the steady-state approximation, with consideration of mass flux conservation, this equation can be simplified as

$$\frac{\partial^3 \zeta}{\partial x^3} - \frac{\rho v_0^2}{\sigma H} \frac{\partial \zeta}{\partial x} = \frac{3}{2LH} - 3v \frac{\rho v_0}{\sigma H^2} - \frac{v_0 j(x, 0)}{\sigma H} \tag{6}$$

The boundary conditions for this task are given by  $\zeta = 0$  at  $x = 0$ ,  $\frac{\partial \zeta}{\partial x}|_{x=0} = 0$ ,  $\frac{\partial \zeta}{\partial x}|_{x=L} = 0$ .

Solution of this problem can be written as

$$\zeta = A \frac{H^2}{G} x + A \left( \frac{H^2}{G} \right)^{3/2} \frac{2 - \exp \sqrt{\frac{G}{H^2}} L - \exp \left( -\sqrt{\frac{G}{H^2}} L \right)}{\exp \sqrt{\frac{G}{H^2}} L - \exp \left( -\sqrt{\frac{G}{H^2}} L \right)} - A \left( \frac{H^2}{G} \right)^{3/2} \frac{1 - \exp \left( -\sqrt{\frac{G}{H^2}} L \right)}{\exp \sqrt{\frac{G}{H^2}} L - \exp \left( -\sqrt{\frac{G}{H^2}} L \right)} \exp \sqrt{\frac{G}{H^2}} x - A \left( \frac{H^2}{G} \right)^{3/2} \frac{1 - \exp \left( \sqrt{\frac{G}{H^2}} L \right)}{\exp \sqrt{\frac{G}{H^2}} L - \exp \left( -\sqrt{\frac{G}{H^2}} L \right)} \exp \left( -\sqrt{\frac{G}{H^2}} x \right) \quad (7)$$

where  $G = \frac{\rho v_0^2 H}{\sigma}$ ,  $A = -\frac{3}{2LH} + 3v \frac{\rho v_0}{\sigma H^2} + \frac{v_0 j(x,0)}{\sigma H}$ .

At the rear part of the melt pool at  $x = L$  for the value of  $\zeta$ , we get

$$\zeta|_{x=L} = A \left( \frac{H^2}{G} \right)^{3/2} \left[ \sqrt{\frac{G}{H^2}} \frac{L}{H} + 2 \frac{1 - \text{Ch} \left( \sqrt{\frac{G}{H^2}} \frac{L}{H} \right)}{\text{Sh} \left( \sqrt{\frac{G}{H^2}} \frac{L}{H} \right)} \right] \quad (8)$$

Let us analyze this expression. Depending on the sign of “A,” which depends on what is more—underestimation of the surface due to thermocapillary acceleration of the melt flow or its overstating caused by the input of a new material with a gas-powder jet; formation of dimple and humps on melt pool surface is possible. The height of the hump, depending on the speed of the process and the length of the melt pool, can significantly exceed the depth of the melt pool H. Such modes are most dangerous from the point of view of unstable surface formation, but it is impossible to analyze this case using the approximations of the “boundary layer” and the smallness of “ $\zeta$ .” This analysis is a theoretical description of the process of forming the profile of the melt pool surface, taking into account the capillary phenomena and the flow of material that the gas-powder jet brings. For the analysis of nonstationary phenomena leading to instability of the growing process, it is necessary to keep the “nonstationary” terms with time derivatives in the equations and to analyze the stability of the “quasi-stationary” behavior.

We derive an equation describing the dynamic behavior of the local excess of the “ $\zeta$ ” melt pool surface above the “quasi-stationary” surface calculated above. We use the nonstationary Navier-Stokes Eq. (5) and the continuity of the flow Eq. (4) for this purpose. Suppose that

$$v_x(x, t) = v_0(x) + v_1(x, t) \quad (9)$$

assuming that  $v_1(x, t) \ll v_0(x)$ . Then, obviously,

$$\zeta(x, t) = \zeta(x) + \zeta_1(x, t) \quad (10)$$

where  $\zeta(x)$  is given by expression Eq. (7). Taking this into account, we obtain from Eq. (10)

$$\frac{\partial v_1}{\partial x} \approx \frac{1}{H} \frac{\partial \zeta_1}{\partial t} + \frac{1}{H\rho} \frac{\partial j(x)}{\partial x} \zeta_1 \quad (11)$$

After substitution of Eqs. (8) and (9) to Eq. (4), taking into account Eq. (10) and the fact that for  $v_0$  and  $\zeta$  expression Eq. (4) is identity, one can obtain an equation for nonstationary addition for flow velocity:

$$\frac{\partial v_1}{\partial t} + v_0 \frac{\partial v_1}{\partial x} + v_1 \frac{\partial v_0}{\partial x} = -\frac{\sigma}{\rho} \frac{\partial^3 \zeta_1}{\partial x^3} + \frac{\sigma}{\rho b^3} \frac{\zeta \partial \zeta_1}{\partial x} + \frac{\sigma}{\rho b^3} \frac{\zeta_1 \partial \zeta}{\partial x} - 3v \frac{v_1}{H^2} \quad (12)$$

By differentiating this equation with respect to (x), taking into account Eq. (11), giving similar and neglecting small terms, we arrive to an equation that describes the dynamic behavior of the excess of the growing surface over a stationary value:

$$\frac{\partial^2 \zeta_1}{\partial t^2} = \frac{\sigma H}{\rho} \frac{\partial^4 \zeta_1}{\partial x^4} - \frac{\sigma H^2}{2\rho b^3} \frac{\partial^2 \zeta_1}{\partial x^2} - \frac{\partial \zeta_1}{\partial x} \left( 2 \frac{\sigma H^2}{\rho b^3 L} - \frac{v_0}{\rho} \frac{\partial j}{\partial z} \right) + \zeta_1 \frac{\partial j}{\partial z} \left( \frac{3v}{H^2 \rho} + \frac{1}{\rho} \frac{\partial v_0}{\partial x} \right) \quad (13)$$

where  $L$  is the length of the melt pool, which is determined from the solution of the heat task.

We use the linear theory of stability and look for the solution of this equation in the form  $\zeta_1 = \zeta_0 \exp(i(\omega t - kx))$ , where  $\zeta_0$  is the constant amplitude and  $\omega$  in turn can be represented as  $\omega = \Omega + i\gamma$ , where  $\Omega$  is the true frequency and  $\gamma$  is the increment (or decrement) of oscillations. Substituting these projects into Eq. (13), we obtain the characteristic equation, which, by neglecting the short-wave capillary ripple in the first approximation, the effect of the viscosity of the melt and the change in its flow velocity due to the thermocapillary effect, we obtain:

$$\Omega \approx \sqrt{\frac{\sigma}{2\rho} \frac{Hk}{b^3}}, \quad (14)$$

$$\gamma = -\frac{b^3}{\sqrt{\frac{\sigma}{2\rho} H}} \left( 2 \frac{\sigma H^2}{\rho b^3 L} - \frac{v_0}{\rho} \frac{\partial j}{\partial z} \right) \quad (14)$$

Thus, we come to the conclusion that, for  $\gamma < 0$ , an oscillatory instability with frequency  $\Omega$  and an increment  $\gamma$  occurs at the surface and for  $\gamma > 0$  the oscillations will decay with the decrement  $\gamma$ . The condition of stability, obviously, is the fulfillment of the inequality:

$$2 \frac{\sigma H^2}{v_0 b^3 L} < \frac{\partial j}{\partial z} \quad (15)$$

Thus, the critical value determining the stability (or instability) of the process of growing is the magnitude of the gradient of the particle flux density in the gas-powder jet along the normal to

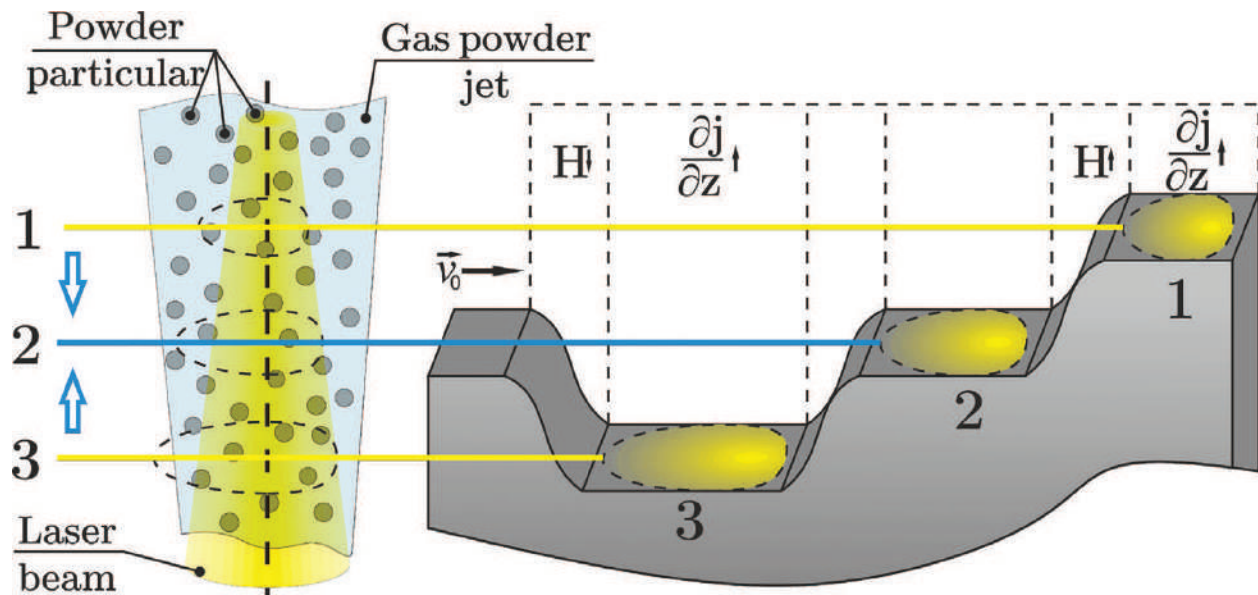


Figure 2. Scheme of stabilization process.

the growing surface. This fact is easy to understand – to stabilize the position of the surface, it is necessary that when it moves upward relative to a stationary value, it would fall under a less dense stream of particles, which would reduce the thickness of the deposited layer, and with shifts downward, under a denser flow, which would increase its thickness and, accordingly, would extinguish the perturbations that arise, as shown in **Figure 2**.

Obviously, for the stability of the process, it is also necessary that the length of the zone in which condition Eq. (15) is satisfied should be greater than the thickness of the layer deposited in one pass. In quantitative analysis, it should also be taken into account that not all particles adhere to the growing surface, so it is necessary to have a gradient value somewhat larger than that given by expression Eq. (15). Thus, a linear analysis of the stability of the process of direct laser deposition process allows us to conclude that stable growth is possible only at the position of the grown surface above the waist of the gas-powder jet, and the necessary condition for stability is the fulfillment of inequality Eq. (15).

### 3. Technology and equipment of direct laser deposition process

Direct laser deposition technology makes it possible to create complex parts and structures in a single technological step without the use of additional equipment, rigging, and adjustment of equipment [8, 21]. It is a complex technology, which is characterized by a multitude of process parameters. All the variety of parameters can be divided into managed and unmanaged [22]. Managed factors include process parameters such as laser power, nozzle type, traverse speed, powder feeding, spot diameter, layer height, powder fraction, selectable path, and rowing thick walls; it is also necessary to take into account the value of their overlap. Process could proceed in high purity Ar atmosphere for sensitive materials as titanium alloys. Also it is possible to get product under local protective atmosphere for less sensitive materials like some stainless steels. Uncontrollable factors include environmental pressure and other physical

conditions of the environment and quality of the raw powder materials. Especially it is necessary to take into account the thermophysical and technological properties of powder alloys.

Direct laser deposition is a multiparameter process; therefore the results of the process are affected by a complex of technological parameters [8, 23]. Among these parameters, it is possible to identify the main characteristics, which primary determine the course of the process [24]. The basic part of process parameters is described in **Table 1**, where the first four points are the main parameters.

On the basis of theoretical and experimental studies, equipment (**Figure 3**) was developed, which realizes DLD process. This is the first Russian equipment for realization of direct laser deposition technology.

The technology realized with this equipment solves a number of problems for modern engineering, improves process efficiency by 10 times, and reduces the cost of manufacturing parts by 3–5 times. Benefits of implementing the DLD are:

- Productivity of manufacturing parts with complex shapes from intractable materials increases.
- Full automation and “digitalization” of manufacturing.
- Raw material consumption decreases.
- Cost saving.
- Enhancement of technological and engineering capabilities.

The equipment is universal, and based on the principle of modular construction, without using accessory devices and bed structures, it is possible to obtain details of any designs and complexity at the request of the customer. The developed equipment can be operated in a chamber filled with protective gas, which completely eliminates the oxidation of metallic

Process parameters	Productivity	Process stability	Usage rate	Roughness	Depth penetration
Laser power	Minor	Minor	Major	Minor	Major
Spot diameter	Major	Minor	Major	Minor	Major
Traverse speed	Major	Major	Major	Minor	Major
Powder feeding	Major	Major	Minor	Minor	Major
Layer height	Minor	Major	Minor	Major	Minor
Shielding gas rate	—	—	Major	Minor	—
Powder fraction	Minor	—	Major	Major	—
Distance between Nozzle and focus of gas-powder jet	Major	Major	Major	Minor	Minor

**Table 1.** Process parameters of direct laser deposition technology.

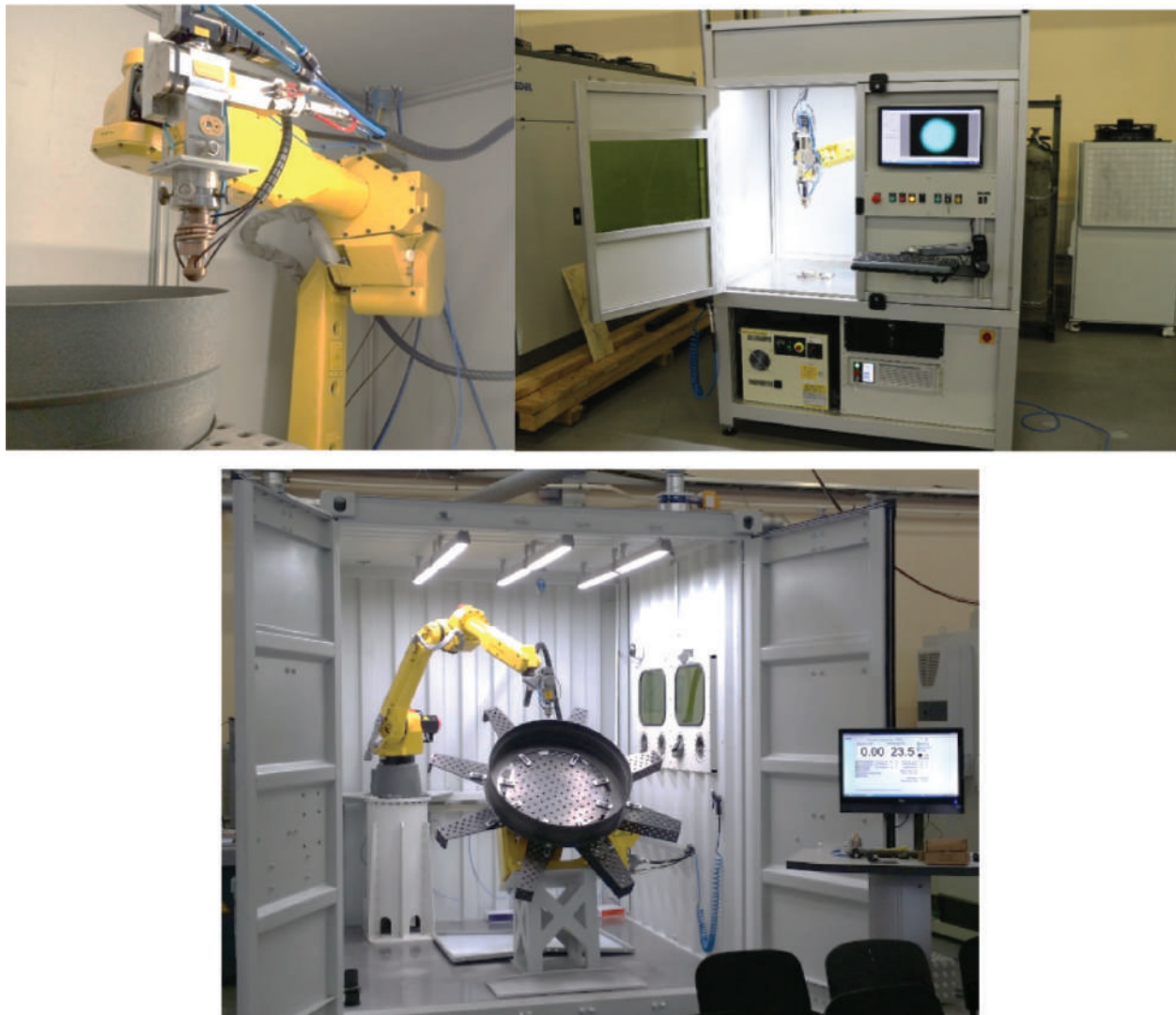


**Figure 3.** Developed equipment for realization of DLD technology.

materials. A technological tool that combines a laser optical head and a powder nozzle is mounted on an industrial robotic manipulator [23]. As a result, the maximum size of the manufactured product is unlimited. The positioner table used for moving the product is also engaged to increase the technology's capabilities.

During the development of the equipment, special attention was paid to the design of the nozzle [24, 25]. It forms a gas-powder jet and thus has determining effect on DLD process. In the investigations, two types of nozzles were used (**Figure 4**): axisymmetric (or coaxial) and axially asymmetric (lateral or non-axial).

The main disadvantage of the lateral nozzle is shape constancy of deposited layer only in one direction, for example, straight line with moving laser head or the body of rotation with rotating substrate (**Figure 4a**). Therefore, despite its high productivity, it is almost used in the manufacture of equipment. For the developed equipment, the four-jet and annular gap powder nozzles were used.

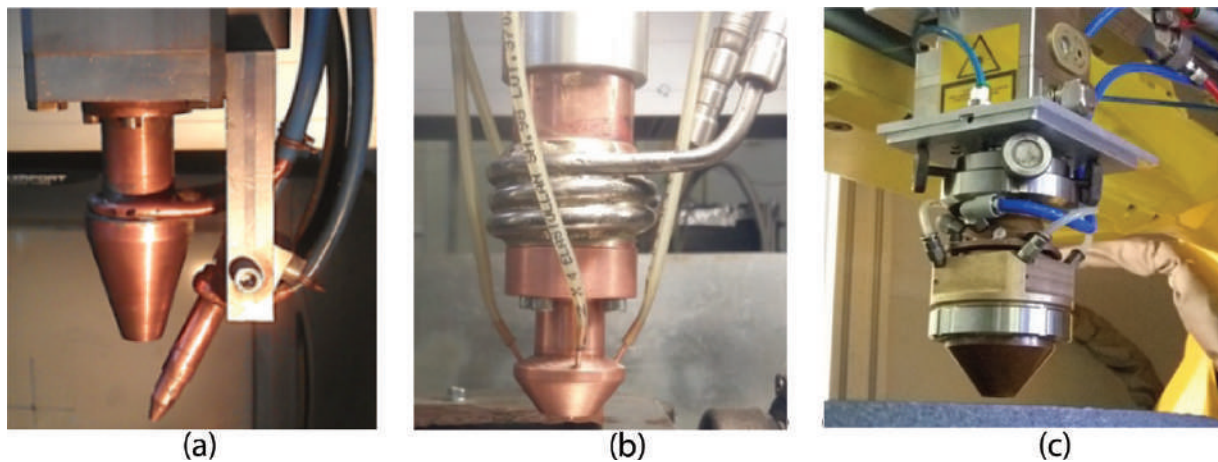


**Figure 4.** Lateral nozzle (a), coaxial four-jet nozzle (b), and coaxial annular gap nozzle (c).

Technological heads equipped with coaxial nozzles are characterized by independence of technological parameters from the direction of tool movement. This allows using complex processing trajectories and obtaining products with complex geometry. Multiple jet nozzles have from three up to six separate channels, which form powder jets. Its design is more complex but allows more flexibility for powder jet control (**Figure 4b**). During processing, the junction area of jets is located near molten pool, which is formed by a laser beam passing through the central hole of the nozzle. Annular gap nozzles are more technologically advanced (**Figure 4c**). Gas-powder jet is supplied through a gap between two conical surfaces that direct and focus it. Due to the uniform distribution of the powder along the circumference of the annular gap, a high degree of symmetry and isotropy with respect to the direction of motion is achieved. The developed nozzles were used to make a number of machines that realize DLD process.

As a result of the theoretical, technological, and design work, a general principle of constructing the equipment was carried out (**Figure 5**).

Below the components of the complex for the implementation of the direct laser deposition process are listed:

1. The two-axis positioner
2. Working chamber
3. Laser head
4. The robotic manipulator
5. Preparation and supplying gas system
6. Gas cleaning and drying device
7. The fiber laser
8. Chiller



nickel, iron, and titanium [8, 21, 26, 27]. Using optimal parameters of DLD process allows preparing samples without such macrodefects as cracks and pores (**Figure 6**).

However, in case of violation of the selected modes, porosity, cracks, and lack of fusion may appear. The main reason for the occurrence of large pores (more than 100  $\mu\text{m}$ ) is the low quality of the shielding gas or work with local protection. Smaller pores could appear because of low quality of powder [21]. Powders obtained by plasma rotating electrode process (PREP) allow to produce samples of lower porosity as compared with the gas atomization. Powders obtained by gas atomization may contain internal pores. It is also possible for them to form with improperly selected modes, which lead to too high cooling rates. Examples of pores in the samples are shown in **Figure 7**.

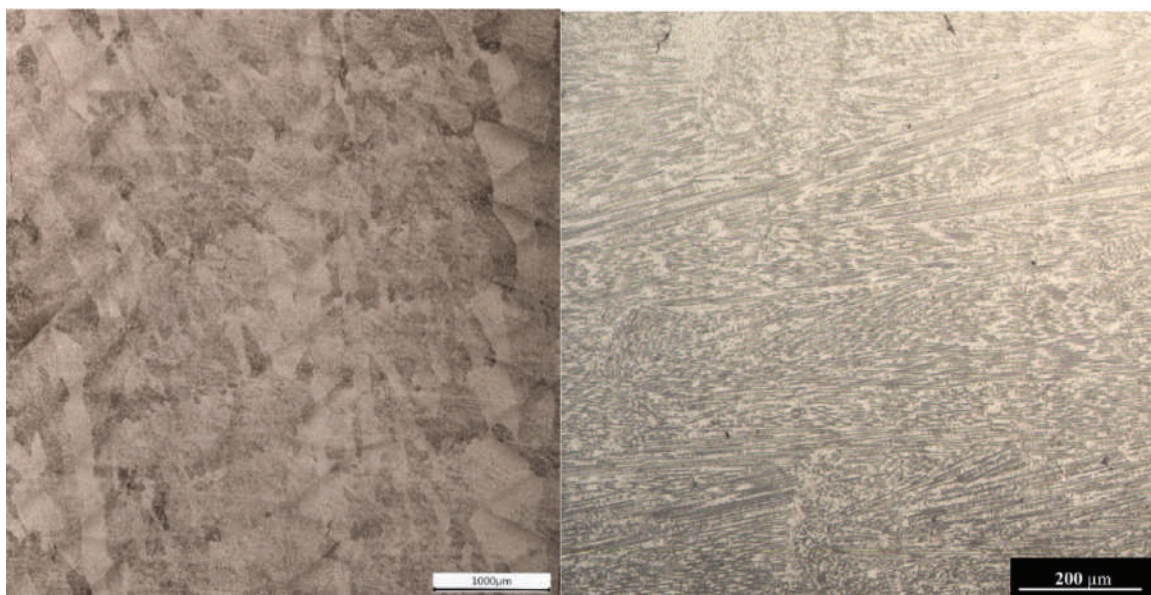


**Figure 6.** Deposited samples without macrodefects: left—Ti-based alloy and right—Ni-based alloy.

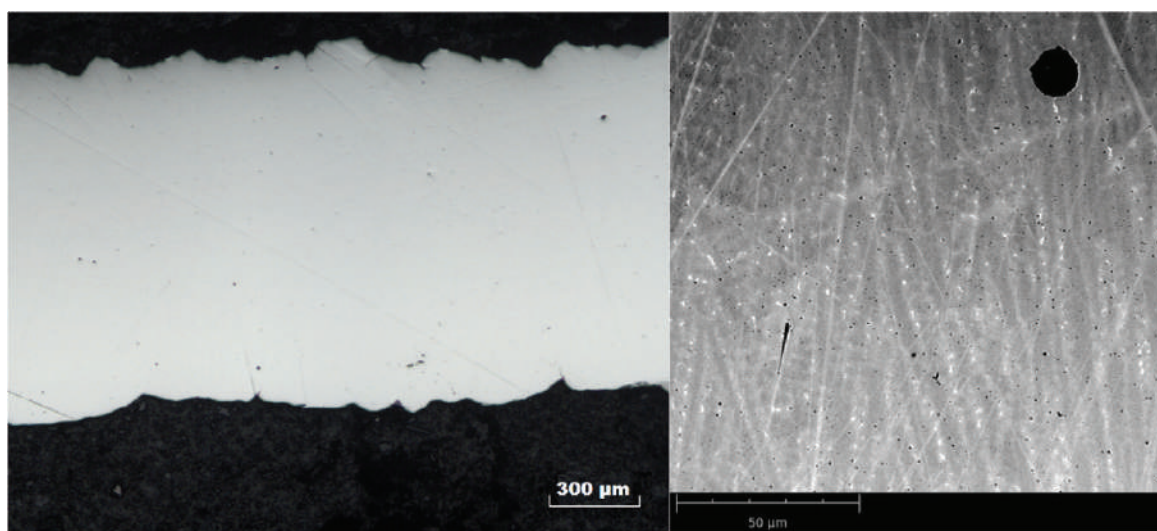


**Figure 7.** Pores in samples, material Ni-based alloy Inconel 625.

Most often defects are lack of fusion, which have a more negative effect on mechanical characteristics than pores. Small lack of fusion results because of using oxidized powder or contaminated powder. Also, their number increases significantly using local protection, rather than full filling the chamber with shielding gas. Examples of lack of fusion are shown in **Figure 8**.

Lack of fusion is also detected at the deposition of thick-walled products. The appearance of such lack of fusion is due to the lack of energy. They are found in the samples grown at low power, a small size of spot diameter. The size of the overlapping layers also affects, but it has less influence and strongly depends on spot diameter. In **Figure 9** lacks of fusion in thick-walled samples are shown.

In the process of deposition, cracks can also appear, especially in those nickel alloys that are prone to their appearance. For all products obtained by direct laser deposition process, the cracks are an impermissible defect; such products are rejected.

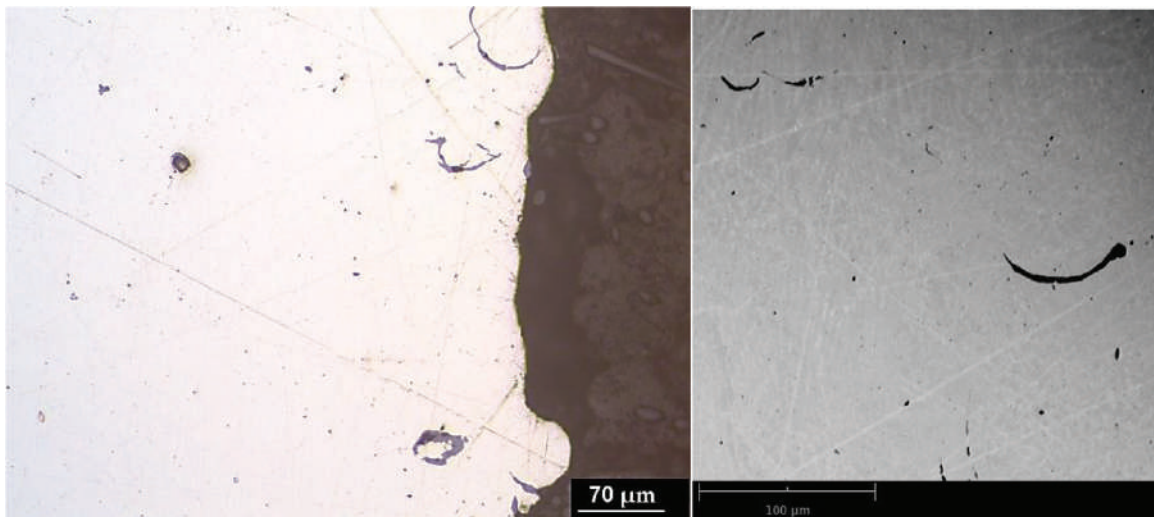


**Figure 8.** Lacks of fusion in samples, material Ni-based alloy Inconel 625.

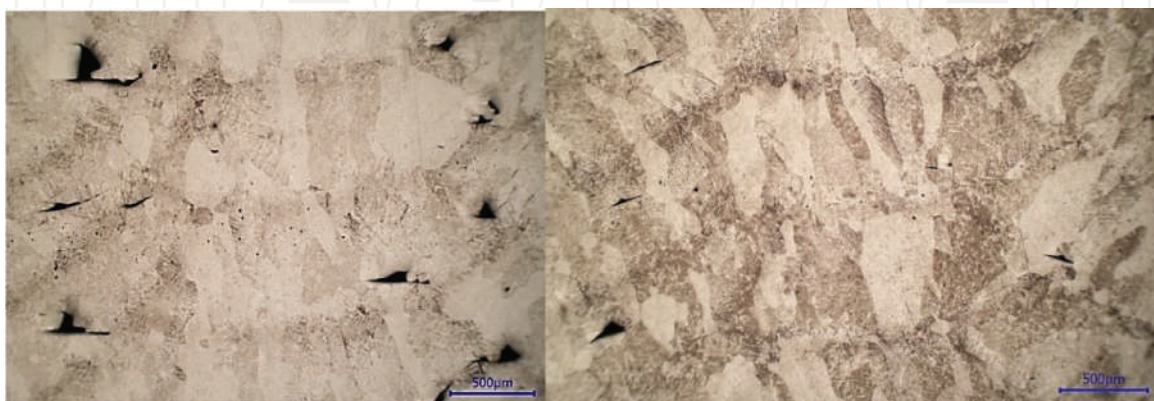


**Figure 9.** Lacks of fusion in thick-walled sample, material Ti-based alloy Grade 5.

The microstructure of the samples obtained has a finely dispersed, predominantly cast structure. Features of structure formation for the different metal alloys using this technology were studied in detail by the authors. The results of research presented by the

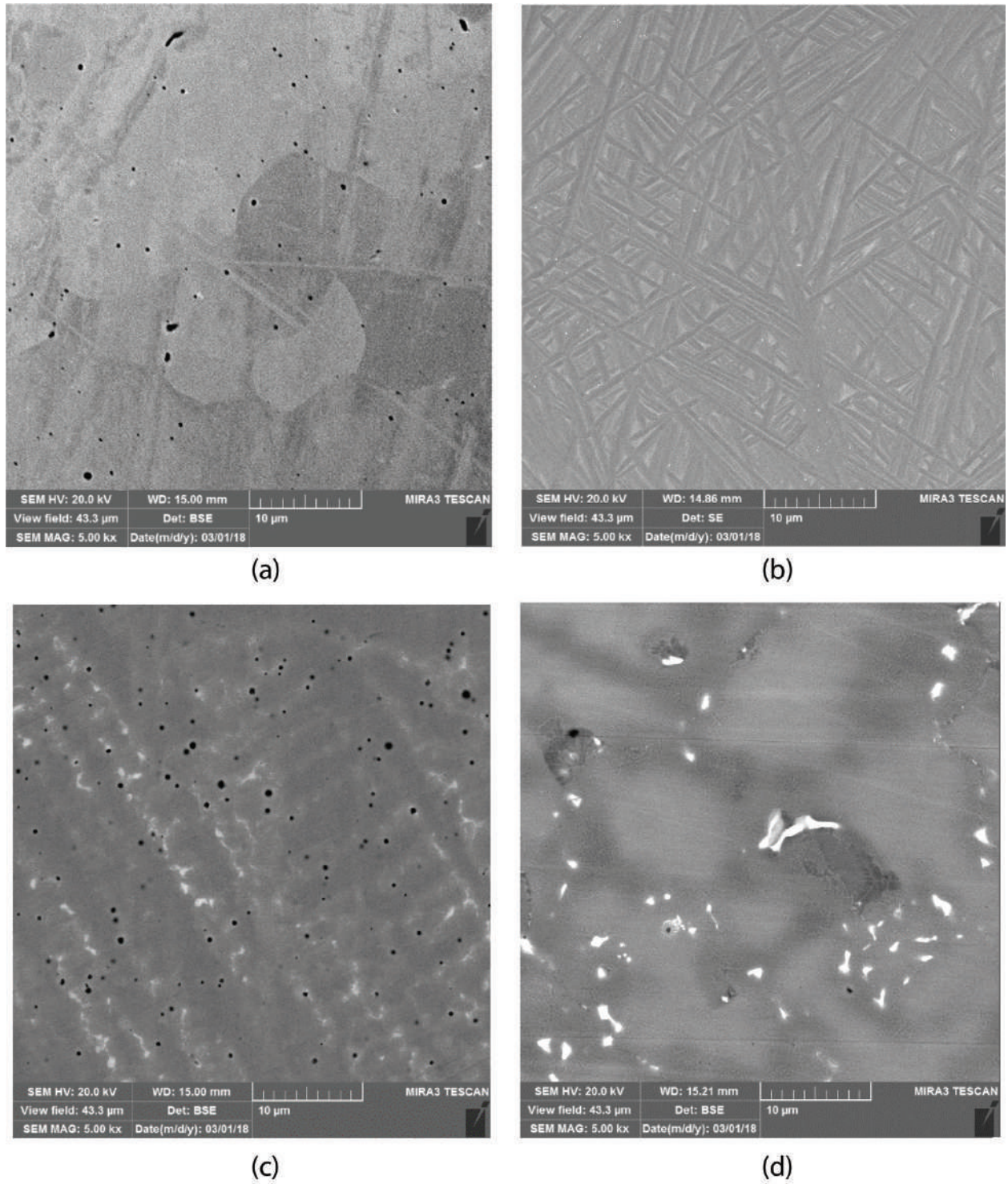


**Figure 10.** Microstructure of deposited samples: (a) 316 L steel, (b) Ti-based alloy analog Grade 35, (c) Inconel 625, and (d) Ni-based alloy analogue Mar-M200.

Material	Yield strength (0,2% Offset), MPa	Ultimate Tensile strength, MPa	Elongation, %
Inconel 625, DLD	489	865	28.5
Inconel 625, cast [31]	310	800	25
Analogue Mar-M200 alloy, DLD	1046	1353	11.5
Analogue Mar-M200 alloy, cast	1075	1108	2.9
Analogue Grade 35 alloy, DLD	882	968	6.6
Analogue Grade 35 alloy, cast	876	951	6.4
Analogue Grade 5 alloy, DLD	1040	1120	8
Analogue Grade 5 alloy, cast	—	880	4
316 L, DLD	272.5	570	41
316 L, cast [31]	177	441	25

**Table 2.** Mechanical characteristics of deposited and cast samples.

authors in the articles [26–30]. In **Figure 10** microstructure of different alloys is presented.

Comparing with cast samples, the products that are manufactured by direct laser deposition technology have ultrafine structure. It provides high level of mechanical characteristics (**Table 2**). Mechanical tests were conducted for a greater number of different alloys; the main results are given in **Table 2**. The materials were tested on uniaxial tension; universal testing machine Zwick/Roell Z250 Allround was used.

## 5. Conclusions

The results of researches show that the developed technology of direct laser deposition, in spite of its technological complexity, can replace the currently used technologies, providing multiple increases in productivity and material saving.

- Direct laser deposition is technology for manufacturing of details with complex form from powder materials using 3D model. It has potential use for different materials in a single part and obtaining details with gradient properties. Using equipment, which realizes this technology, it is possible to produce details of any size.
- The process productivity is 10 times higher in comparison with layered synthesis technologies like SLM. Mechanical properties of the obtained products are much higher than the characteristics of the cast metal; there are no pores and cracks and is no lack of fusion.
- This equipment has a maximum capacity in comparison with existing analogues: up to 2.5 kg/h for metallic materials.
- This is the first Russian technology and equipment for the implementation of additive production.

## Author details

Gleb Turichin\* and Olga Klimova-Korsmik

\*Address all correspondence to: gleb@ltc.ru

State Marine Technical University, Saint-Petersburg, Russian Federation

## References

- [1] Gu D. New metallic materials development by laser additive manufacturing. In: *Surface Engineering*. New-York: Elsevier Ltd; 2015. pp. 163-180
- [2] Kianiana B, Tavassoli S, Larsson TC. The role of additive manufacturing technology in job creation: An exploratory case study of suppliers of additive manufacturing in Sweden. In: *Procedia CIRP, 12th Global Conference on Sustainable Manufacturing – Emerging Potentials*, Vol. 26; 2015. pp. 93-98
- [3] Gress DR, Kalafsky RV. Geographies of production in 3D: Theoretical and research implications stemming from additive manufacturing. *Geoforum*. 2015;**60**:43-52
- [4] Siemieniuch CE, Sinclair MA, de Henshaw MJC. Global drivers, sustainable manufacturing and systems ergonomics. *Applied Ergonomics*. 2015;**51**:104-119
- [5] Evers DR, Potter AT. Industrial additive manufacturing: A manufacturing systems perspective. *Computers in Industry*. 2017;**92–93**:208-218
- [6] Liverani E, Toschi S, Ceschini L, Fortunato A. Effect of selective laser melting (SLM) process parameters on microstructure and mechanical properties of 316L austenitic stainless steel. *Journal of Materials Processing Technology*. 2017;**249**:255-263
- [7] Olakanmi EO, Cochrane RF, Dalgarno KW. A review on selective laser sintering/melting (SLS/SLM) of aluminum alloy powders: Processing, microstructure, and properties. *Progress in Materials Science*. 2015;**74**:401-477
- [8] Turichin GA, Klimova OG, Zemlyakov EV, Babkin KD, Kolodyazhnyy DY, Shamray FA, Travyanov AY, Petrovskiy PV. Technological aspects of high speed direct laser deposition based on heterophase powder metallurgy. *Physics Procedia*. 2015;**78**:397-406
- [9] Wilson MJ, Piya C, Shin YC, Zhao F, Ramani K. Remanufacturing of turbine blades by laser direct deposition with its energy and environmental impact analysis. *Journal of Cleaner Production*. 2014;**80**:170-178
- [10] Thompsona SM, Bianc L, Shamsaiea N, Yadollahi A. An overview of direct laser deposition for additive manufacturing; Part I: Transport phenomena, modeling and diagnostics. *Additive Manufacturing*. 2015;**8**:36-62

- [11] Dutta B, Palaniswamy S, Choi J, Song LJ, Mazumder J. Additive manufacturing by direct metal deposition. *Advanced Materials & Processing*. 2011;**169**:33-36
- [12] Renderos M, Girot F, Lamikiz A, Torregaray A, Saintier N. Ni based powder reconditioning and reuse for LMD process. *Physics Procedia*. 2016;**83**:769-777
- [13] Wang Y, Tang H, Fang Y, Wang H. Microstructure and mechanical properties of hybrid fabricated 1Cr12Ni2WMoVNb steel by laser melting deposition. *Chinese Journal of Aeronautics*. 2013;**26**(2):481-486
- [14] Saboori A, Gallo D, Biamino S, Fino P, Lombardi M. An overview of additive manufacturing of titanium components by directed energy deposition: Microstructure and mechanical properties. *Applied Sciences*. 2017;**7**:883-906
- [15] Zhong C, Gasser A, Kittel J, Wissenbach K, Poprawe R. Improvement of material performance of Inconel 718 formed by high deposition-rate laser metal deposition. *Materials and Design*. 2016;**98**:128-134
- [16] Turichin GA. Hydrodynamic stability aspects of gas-vapour channel at energy beam welding. *Physics and Chemistry of Metal Treatment*. 1996;**4**:74-81
- [17] Reisgen U, Schleser M, Abdurakhmanov A, Turichin GA, Valdaytseva EA, Bach F-W, Hassel T, Beniyash A. Study of factors affecting defect formation of the weld seam at electron-beam welding in outer space. *Avtomaticheskaya Svarka*. 2012;**2**:13-20
- [18] Matsunawa A, Kim J-D, Seto N, Mizutani M, Katayama S. Dynamics of keyhole and molten pool in laser welding. *Journal of Laser Applications*. 1998;**10**(6):247-254
- [19] Raisgen U, Schlezler M, Abdurachmanov A, Turichin G, Valdaytseva E, Bach F-W, Hassel T, Banyash A. Investigation of factors influencing the formation of weld defects in non-vacuum electron beam welding. *Paton Welding Journal*. 2012;**2**:11-18
- [20] Kumar A, Roy S. Effect of three-dimensional melt pool convection on process characteristics during laser cladding. *Computational Materials Science*. 2009;**46**(2):495-506
- [21] Glukhov V, Turichin G, Klimova-Korsmik O, Zemlyakov E, Babkin K. Quality management of metal products prepared by high-speed direct laser deposition technology. *Key Engineering Materials*. 2016;**684**:461-467
- [22] Turichin GA, Somonov VV, Klimova OG. Investigation and modeling of the process of formation of the pad weld and its microstructure during laser cladding by radiation of high power fiber laser. *Applied Mechanics and Materials*. 2014;**682**:160-165
- [23] Turichin GA, Somonov VV, Babkin KD, Zemlyakov EV, Klimova OG. High-speed direct laser deposition: Technology, equipment and material. In: *IOP Conference Series: Materials Science and Engineering Current Problems and Solutions*, Vol. 125; 2016. p. 012009
- [24] Turichin G, Zemlyakov E, Klimova O, Babkin K. Hydrodynamic instability in high-speed direct laser deposition for additive manufacturing. *Physics Procedia*. 2016;**83**:674-683

- [25] Korsmik RS, Turichin GA, Babkin KD. Laser cladding technological machine. Investigation of efficiency of various nozzles design. *Journal of Physics: Conference Series*. 2017; **857**:4
- [26] Sklyar MO, Turichin GA, Klimova OG, Zotov OG, Topalov IK. Microstructure of 316L stainless steel components produced by direct laser deposition. *Steel in Translation*. 2016; **46**(12):883-887
- [27] Sklyar MO, Klimova-Korsmik OG, Cheverikin VV. Formation structure and properties of parts from titanium alloys produced by direct laser deposition. *Solid State Phenomena*. 2017;**265**:535-541
- [28] Klimova-Korsmik OG, Turichin GA, Zemlyakov EV, Babkin KD, Travyanov AY, Petrovskiy PV. Structure formation in Ni superalloys during high-speed direct laser deposition. *Physics Procedia*. 2016;**83**:716-722
- [29] Klimova-Korsmik OG, Turichin GA, Zemlyakov EV, Babkin KD, Petrovskiy PV, Travyanov AY. Structure formation in Ni superalloys during high-speed direct laser deposition. *Materials Science Forum*. 2017;**879**:978-983
- [30] Turichin GA, Travyanov AY, Petrovskiy PV, Zemlyakov EV, Kovac M, Vondracek S, Kondratiev A, Khvan AV, Cheverikin VV, Ivanov DO, Bazhenova IA, Dinsdale AT. Prediction of solidification behaviour and microstructure of Ni based alloys obtained by casting and direct additive laser growth. *Materials Science and Technology*. 2016;**32**(8): 746-751
- [31] DebRoy T, Wei HL, Zuback JS, Mukherjee T, Elmer JW, Milewski JO, Beese AM, Wilson-Heid A, De A, Zhang W. Additive manufacturing of metallic components—Process, structure and properties. *Progress in Materials Science*. 2018;**92**:112-224